

Double Asteroid Redirection Test (DART): Structural and Dynamic Interactions between Asteroidal Elements of Binary Asteroid (65803) Didymos

Masatoshi Hirabayashi, Fabio Ferrari, Martin Jutzi, Ryota Nakano, Sabina D Raducan, Paul Sánchez, Stefania Soldini, Yun Zhang, Olivier S Barnouin, Derek C Richardson, et al.

▶ **To cite this version:**

Masatoshi Hirabayashi, Fabio Ferrari, Martin Jutzi, Ryota Nakano, Sabina D Raducan, et al.. Double Asteroid Redirection Test (DART): Structural and Dynamic Interactions between Asteroidal Elements of Binary Asteroid (65803) Didymos. The Planetary Science Journal, 2022, 3, 10.3847/psj/ac6eff . hal-03733073

HAL Id: hal-03733073
https://hal.science/hal-03733073

Submitted on 21 Jul 2022

HAL is a multi-disciplinary open access archive for the deposit and dissemination of scientific research documents, whether they are published or not. The documents may come from teaching and research institutions in France or abroad, or from public or private research centers.

L'archive ouverte pluridisciplinaire **HAL**, est destinée au dépôt et à la diffusion de documents scientifiques de niveau recherche, publiés ou non, émanant des établissements d'enseignement et de recherche français ou étrangers, des laboratoires publics ou privés.

The Planetary Science Journal, 3:140 (20pp), 2022 June https://doi.org/10.3847/PSJ/ac6eff
© 2022. The Author(s). Published by the American Astronomical Society.
OPEN ACCESS

Double Asteroid Redirection Test (DART): Structural and Dynamic Interactions between Asteroidal Elements of Binary Asteroid (65803) Didymos

Masatoshi Hirabayashi[1], Fabio Ferrari[2], Martin Jutzi[2], Ryota Nakano[3], Sabina D. Raducan[2], Paul Sánchez[4], Stefania Soldini[5], Yun Zhang[6,7], Olivier S. Barnouin[8], Derek C. Richardson[9], Patrick Michel[6], Elisabetta Dotto[10], Alessandro Rossi[11], and Andrew R. Rivkin[8]
[1] Department of Aerospace Engineering, Department of Geosciences, Auburn University, Auburn, AL, USA; thirabayashi@auburn.edu
[2] Space Research and Planetary Sciences, Physics Institute, University of Bern, Bern, Switzerland
[3] Department of Aerospace Engineering, Auburn University, Auburn, AL, USA
[4] Colorado Center for Astrodynamics Research, University of Colorado Boulder, 3775 Discovery Drive, Boulder, CO, USA
[5] Department of Mechanical, Materials and Aerospace Engineering, University of Liverpool, Liverpool, UK
[6] Université Côte d'Azur, Observatoire de la Côte d'Azur, CNRS, Laboratoire Lagrange, Nice, France
[7] Department of Aerospace Engineering, University of Maryland, College Park, MD, USA
[8] Johns Hopkins University/Applied Physics Laboratory, Laurel, MD, USA
[9] Department of Astronomy, University of Maryland, College Park, MD, USA
[10] INAF—Osservatorio Astronomico di Roma, I-00100, Italy
[11] Istituto di Fisica Applicata "Nello Carrara" (IFAC-CNR), Sesto Fiorentino I-50019, Italy
Received 2022 February 1; revised 2022 May 3; accepted 2022 May 10; published 2022 June 14

Abstract

NASA's Double Asteroid Redirection Test (DART) mission is the first full-scale planetary defense mission. The target is the binary asteroid (65803) Didymos, in which the smaller component Dimorphos (∼164 m equivalent diameter) orbits the larger component Didymos (∼780 m equivalent diameter). The DART spacecraft will impact Dimorphos, changing the system's mutual orbit by an amount that correlates with DART's kinetic deflection capability. The spacecraft collision with Dimorphos creates an impact crater, which reshapes the body. Also, some particles ejected from the DART impact site on Dimorphos eventually reach Didymos. Because Didymos's rapid spin period (2.26 hr) may be close to its stability limit for structural failure, the ejecta reaching Didymos may induce surface disturbance on Didymos. While large uncertainties exist, nonnegligible reshaping scenarios on Didymos and Dimorphos are possible if certain conditions are met. Our analysis shows that given a surface slope uncertainty on Dimorphos of 45°, with no other information about its local topography, and if the DART-like impactor is treated as spherical, the ejecta cone crosses Didymos with speeds $\gtrsim$14 m s^{-1} in 13% of simulations. Additional work is necessary to determine the amount of mass delivered to Didymos from the DART impact and whether the amount of kinetic energy delivered is sufficient to overcome cohesive forces in those cases. If nonnegligible (but small) reshaping occurs for either of these asteroids, the resulting orbit perturbation and reshaping are measurable by Earth-based observations.

Unified Astronomy Thesaurus concepts: Asteroids (72); Near-Earth objects (1092)

1. Introduction

The NASA Direct Asteroid Redirection Test (DART) mission is the first planetary defense mission to test kinetic impact deflection technology to redirect an asteroid effectively (e.g., Cheng et al. 2018; Rivkin et al. 2021). DART aims to make its spacecraft collide with Dimorphos, the smaller satellite of the S-type binary asteroid (65803) Didymos. For clarity, this paper denotes this binary asteroid as the Didymos–Dimorphos system while calling Didymos the larger primary and Dimorphos the smaller secondary. The spacecraft was successfully launched at 06:21:02 on 2021 November 24 UTC, and the collision with Dimorphos is planned to happen at 23:14 on 2022 September 26 UTC (as of 2022 January). DART's almost head-on collision adds kinetic momentum to Dimorphos, causing it to decelerate and have a shorter semimajor axis and thus a shorter mutual orbit period (Cheng et al. 2016, 2018). This impact event will be observed by LICIACube (Dotto et al. 2021) and ground- and spaced-based telescopes. Four years after the DART impact, ESA's Hera will visit the Didymos–Dimorphos system to fully characterize DART's impact outcome and the physical and compositional properties of the asteroids, including internal and subsurface structures, contributing to both planetary defense and asteroid science and binary formation (P. Michel et al. 2022, in preparation).

The nominal orbital period change driven by the DART impact is expected to be at least ∼73 s (Rivkin et al. 2021), though many factors, in particular the level of cohesion and/or porosity of the target, have a high influence on the outcome (A. M. Stickle et al. 2022, in preparation). The DART deflection efficiency is assessed through the momentum transfer enhancement factor, β, i.e., the ratio of the projectile's momentum summed with the momentum of ejecta produced by the impact to the projectile's momentum (i.e., a completely inelastic collision; e.g., Holsapple & Housen 2012; Cheng et al. 2016, 2018; Rivkin et al. 2021). The β value is determined by comparing the orbital periods of Dimorphos before and after the DART impact, given the detailed trajectory and mass of the spacecraft. If there are no ejecta, β equals 1; i.e., the momentum transferred to the target is only that of the projectile. If impact-driven ejecta depart from the impact site opposite the spacecraft direction, then β is greater than 1, and

Original content from this work may be used under the terms of the Creative Commons Attribution 4.0 licence. Any further distribution of this work must maintain attribution to the author(s) and the title of the work, journal citation and DOI.

its value depends on the momentum carried by the ejecta. At the other extreme, if a shock wave reaches the other side of the impact site, its reflection at the surface may lead to the extraction of ejecta at the antipode along the spacecraft's incoming direction, leading to a β value smaller than 1, though this case is believed unlikely.

The baseline β assessment considers the mutual orbit under the assumption that Didymos and Dimorphos are structurally rigid; in other words, these bodies do not experience any reshaping while dynamically interacting with each other (Cheng et al. 2018). However, recent work suggests that coupling dynamics and structure may affect the momentum transfer if reshaping happens to these bodies (Hirabayashi et al. 2017, 2019a). Multiple factors may control Didymos's reshaping process (Zhang et al. 2017, 2021). The reshaping event then changes the mutual gravitational field, causing additional dynamical perturbation in the Didymos–Dimorphos system. If the reshaping process is large enough to cause an orbital period change greater than the measurement uncertainty of 7.3 s imposed by the DART level 1 requirement (Rivkin et al. 2021), better quantifying the β value requires appropriate assessments of how such a process affects the mutual dynamics after the DART impact. Earth-based observations conducted after the expected reshaping process, which takes hours to complete, can measure the orbital period affected by this process.

Reshaping processes depend on how each body experiences the DART impact. Dimorphos undergoes a cratering process driven by the DART impact (Stickle et al. 2017, 2020; Rainey et al. 2020). While Rainey et al. (2020) suggested a rough estimate of the DART impact-driven crater size as $\sim$2 m diameter for a high-strength case and $\sim$20 m diameter or more for a low-strength case, the crater formation strongly depends on the impact conditions and surface and subsurface strengths (S. D. Raducan & M. Jutzi 2022, in preparation). The development of an impact crater permanently changes Dimorphos's shape. On the other hand, Didymos is currently rotating at a spin period of 2.26 hr (Pravec et al. 2006), and its bulk density is $2170 \pm 350\,\mathrm{kg\,m^{-3}}$ (Naidu et al. 2020). Because of these conditions, the surface slope reaches 90° at latitudes lower than 45° (Naidu et al. 2020), implying tension in the internal structure. If the internal structure is mechanically homogeneous, the body needs cohesive strength to resist structural failure (Zhang et al. 2017, 2021; Naidu et al. 2020). A mechanically strong interior, given cohesion, may allow surface layers to be strengthless, under which centrifugal and gravitational forces do not initiate material movements (Ferrari & Tanga 2022). After the DART impact, ejecta particles depart from the impact site and experience complex dynamics (E. G. Fahnestock et al. 2022, in preparation). Some ejecta particles then fall onto Didymos with various impact speeds, depending on how the ejecta cone evolves (Yu et al. 2017; Yu & Michel 2018). If Didymos receives enough net kinetic energy to cause surface disturbances, material flows may occur, causing reshaping (Hirabayashi et al. 2017).

The primary issue is that because these bodies' physical properties are largely unknown, there is limited information on whether measurable reshaping processes may occur or not for one or both bodies. Therefore, analyses in general need a wide range of parametric assessment to quantify the system's response to the DART impact, challenging rigorous predictions about the reshaping processes. Such uncertainties lead to the following primary question: If measurable reshaping occurs for either Didymos or Dimorphos, how does the resulting orbital perturbation influence the β value?

This question further broadens the area of investigation related to the following four questions.

1. What physical properties control reshaping on Didymos and Dimorphos?
2. If measurable reshaping occurs due to the DART impact, how does the Didymos–Dimorphos system structurally and dynamically respond?
3. If the DART impact does not induce measurable reshaping, how does the current structure remain intact during the impact event?
4. How do the outcomes (both reshaping and non-reshaping) give insights into a binary asteroid's natural dynamical and structural evolution?

These questions are consistent with the DART-4B requirement category (Rivkin et al. 2021).

As part of the preimpact reports from the DART investigation team, we summarize the current efforts to better understand the potential interactions between dynamics and structure after the DART impact. These efforts are aligned with those of the Dynamics Working Group (D. C. Richardson et al. 2022, in preparation) under joint collaborations with other working groups (E. G. Fahnestock et al. 2022, in preparation; M. Pajola et al. 2022, in preparation; P. Pravec et al. 2022, in preparation; A. M. Stickle et al. 2022, in preparation). The major purpose of this paper is to review the current understanding of multiphysics regimes (impact, dynamics, and structure) and visualize the questions regarding the interactions between dynamics and structure driven by the DART impact. This paper is divided into three major sections. Section 2 introduces multiple team efforts related to the reshaping processes on Dimorphos and Didymos. This section also discusses how to measure Didymos's reshaping magnitude. We note that determining Dimorphos's reshaping, i.e., the crater size, may also be possible based on the planned optical measurement of the DART ejecta (E. G. Fahnestock et al. 2022, in preparation; D. C. Richardson et al. 2022, in preparation), though we omit the details of this approach in this study. Section 3 focuses on orbital perturbation driven by reshaping of either Dimorphos or Didymos. The investigations in this section provide the correlation between the orbital period change and the reshaping magnitude. Section 4 provides interpretations of the analyses above. Unless there are explicitly stated definitions, the following discussions use the parameters defined in Table 1 in the main text, while the Appendix also uses the additional parameters defined in Table 2.

2. Reshaping Mechanisms and Processes

2.1. Impact-driven Reshaping on Dimorphos

The crater formation by the DART impact strongly depends on both the impactor's and the target's physical properties and impact conditions (e.g., Stickle et al. 2017; Raducan et al. 2019, 2020; Rainey et al. 2020). Among the recent efforts in characterizing the DART impact are numerical simulations using a smoothed particle hydrodynamics (SPH) impact code (Jutzi et al. 2008; Jutzi 2015). They simulate vertical and oblique DART-like impact scenarios on both spherical and elliptical asteroid targets (S. D. Raducan & M. Jutzi 2022, in

Table 1
Major Physical Parameters Used for Discussions

Notation	Description	Dimensions
ρ_B	Bulk density	M/L^3
ρ_G	Grain density	M/L^3
$T_{\rm sp}$	Didymos spin period	S
$dT_{\rm sp}$	Didymos spin period change	S
dD	Didymos short-axis length change	L
$\omega_{\rm sp}$	Didymos spin rate	$1/S$
U_g	Didymos gravity potential	L^2/S^2
(x, y, z)	Didymos body-fixed frame	L
(ξ, η, ζ)	Dimorphos body-fixed frame	L
dL	Dimorphos short-axis length change	L
θ	Angle of internal friction	[−]
C_0	Bulk cohesive strength	M/LS^2
$C_{\rm crit}$	Critical cohesive strength	M/LS^2
c	Interparticle cohesive strength	M/LS^2
V_x	Particle speed in the surface horizontal direction	L/S^2
V_D	DART impact speed	L/S^2
$V_{\rm ejc}$	Collision speed of DART-driven ejecta on Didymos	L/S^2
M_D	DART spacecraft mass	M
$M_{\rm ejc}$	DART-driven ejecta particle mass	M
$P_{\rm cr}$	Crushing pressure	M/LS^2
ϕ_0	Initial bulk porosity	[−]
ψ_c	Volumetric ratio of strong core to entire body in Didymos	[−]
M_e	Mass ratio of ejected mass to total mass in Didymos	[−]

Note. For dimensions, M is mass, L is length, and S is time.

Table 2
Major Physical Parameters for the Ejecta Speed and Cone Geometry Computation

Notation	Description	Value	Units
g	Gravitational acceleration	4.975×10^{-5}	m s^{-2}
ρ_t	Target bulk density	2170	kg m^{-3}
R_g	Gravity-regime crater radius	45.71	m
R_s	Strength-regime crater radius ($C_0 = 2$ kPa)	14.76	m
C_{Tg}	Gravity-regime crater formation parameter	0.8	[−]
C_{Ts}	Strength-regime crater formation parameter	1.02	[−]
r	Distance from the impact point to the ejecta base	[−]	m
v_f	Ejection speed	[−]	m s^{-1}
ψ_f	Ejection angle	[−]	[−]
r	Distance from the impact point to the ejecta base	[−]	m
μ	Crater scaling parameter	0.41	[−]
ϵ	Stability parameter	1	Pa
ψ_0	Initial ejection angle	$52.^\circ4 \pm 6.^\circ1$	[−]
ψ_d	Ejection angle variation	$18.^\circ4 \pm 8.^\circ2$	[−]
$\phi_{\rm im}$	Impact angle	[−]	[−]
$\theta_{\rm az}$	Azimuth from the impactor incoming direction	[−]	[−]

Note. The quantities represent the DART impact conditions on Didymos. The crater scaling parameters are based on Richardson et al. (2007).

preparation), where the impactor mass, M_D, and the impact speed, V_D, are approximately 500 kg and 6 km s^{-1}, respectively. Throughout the simulations, the pressure-dependent strength model (Collins et al. 2004) describes the material strength, given the cohesive strength, C_0, and the angle of internal friction, θ, as free parameters. The initial target porosity, ϕ_0, is 40% based on the $P-\alpha$ model (Jutzi et al. 2008), and a relatively small crushing strength ($P_{\rm cr} = 10$ MPa) is assumed, which may be a lower bound for material analogs of Dimorphos. With the use of the basalt-like material model, which sets a grain density of $\rho_G = 2650$ kg m^{-3}, the bulk density, ρ_B, is given as 1600 kg m^{-3}.[12]

The DART impact on Dimorphos in the gravity regime is an end-member of the expected impact condition, which is comparable to the artificial crater formation on Ryugu found by Hayabusa2's SCI impact (Arakawa et al. 2020). Within this regime, cohesionless surface and subsurface layers may make the impact process subcatastrophic, where the target body significantly changes its shape but does not experience catastrophic disruption (e.g., Jutzi 2019). The SPH simulations for up to ∼2 hr after the DART impact reveal that for weak asteroid targets with $C_0 < 10$ Pa, a DART-like impact creates morphologies dissimilar to a typical impact crater but induces significant shape deformation. Figure 1 shows the initial target shape, a spherical, 150 m diameter body with $C_0 = 0$ Pa and $\theta = 31^\circ$, and the shape 2 hr after a vertical DART-like impact on it. The deformation may lead to an axis change up to ∼30 m along the impact direction.

The SPH simulations also predict variations in the net momentum of ejecta depending on the target cohesion. For example, for an impact on targets with $C_0 > 10$ Pa, most ejecta acquire speeds higher than Dimorphos's escape speed, 0.1 m s^{-1}. On the other hand, a lower C_0 leads to more ejecta below the escape speed and a larger redistribution of material within the body, giving an overall shape change. Furthermore, previous studies (e.g., Housen et al. 2018) argue that the target crushing pressure affects the net momentum of ejecta. When this quantity is high, energy loss due to material crushing is less, causing an efficient energy transfer to the material's kinetic energy and thus more ejecta with higher speeds.

2.2. Rotationally Driven Reshaping on Didymos

Top-shaped asteroids, or relatively spheroidal bodies with an equatorial ridge, rotate with relatively short spin periods and are common among near-Earth asteroids (NEAs; Taylor et al. 2012; Benner et al. 2015). Because many top shapes, like the primary of (66391) Moshup, an S-type system formerly known as 1999 KW4 (Ostro et al. 2006), are uniquely axisymmetric (e.g., Benner et al. 2015), the preferred explanation is that their shape results from rotational reshaping (e.g., Walsh et al. 2008; Harris et al. 2009). Some top-shaped NEAs, including Moshup, host smaller satellites (e.g., Becker et al. 2015; Naidu et al. 2015), suggesting that top-shape formation and evolution strongly correlate with binary and multiple system formation (Margot et al. 2015; Walsh & Jacobson 2015). Such formation processes cause their unique binary configuration evolution cycles (Jacobson & Scheeres 2011; Jacobson et al. 2016).

Detailed observations of asteroids (101955) Bennu and (162173) Ryugu by OSIRIS-REx (Lauretta et al. 2019) and

[12] This bulk density value is lower than the estimated bulk density, 2170 kg m^{-3}. Nevertheless, we use this quantity to demonstrate what the subcatastrophic regime looks like.

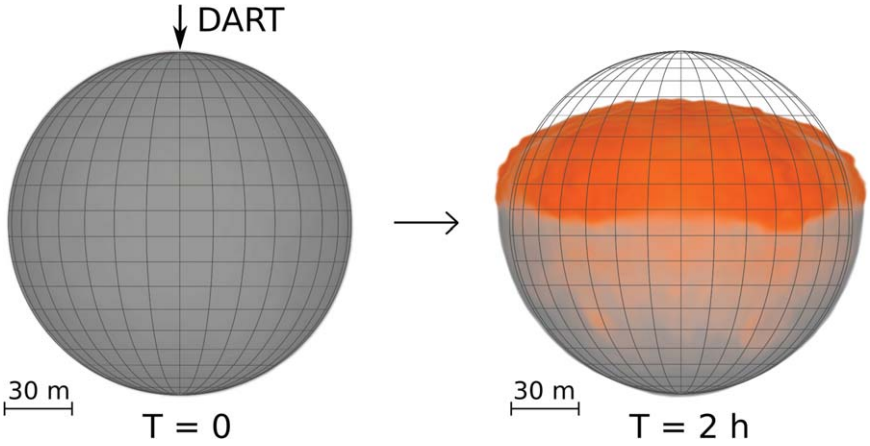


Figure 1. Initial (left) and final (right) asteroid morphology derived from an SPH simulation of a vertical DART-like impact on a spherical, 150 m diameter body with $C_0 = 0$ Pa and $\theta = 31°$. The orange regions indicate materials transported from their original locations to new places due to the DART impact. The bulk density, ρ_B, is 1600 kg m^{-3}.

Hayabusa2 (Watanabe et al. 2019), respectively, broadened discussions about the formation and evolution mechanisms of top shapes, such as rotational reshaping (Hirabayashi et al. 2019b, 2020a; Cheng et al. 2020), catastrophic disruption of parent bodies followed by reaccumulation of debris (Michel et al. 2020), and accumulation of ejected debris while bodies spin at fast rotation (Hirata & Ikeya 2021). Unlike other top shapes, however, Bennu and Ryugu are not fast rotators and do not have long-lived natural satellites; Bennu's spin period is 4.296 hr (Hergenrother et al. 2019; Nolan et al. 2019), while Ryugu's is 7.63 hr (Watanabe et al. 2019). If rotation indeed plays a crucial role in their top shapes, the present spin states of these asteroids may not significantly contribute to their rapid top-shape evolution, although surface material flows actively occur (Barnouin et al. 2019; Walsh et al. 2019; Daly et al. 2020; Jawin et al. 2020). If so, their dynamic spin evolution has enhanced their top shapes in the past (Hirabayashi et al. 2019b, 2020a; Walsh et al. 2019).

Didymos is reported to be a top-shaped asteroid with a bulk density, ρ_B, of 2170 kg m^{-3} (Naidu et al. 2020) and a spin period, $T_{\rm sp}$, of 2.26 hr (Pravec et al. 2006). This condition is near the ~2.2 hr spin barrier of a spherical rubble-pile body with $\rho_B = 2200$ kg m^{-3} (Pravec et al. 2008). This fast rotation causes strong centrifugal acceleration on the surface, particularly in the equatorial region. Therefore, at present, this asteroid may be close to or beyond its structural failure, i.e., a complete collapse, without mechanical strength to hold the entire structure (Zhang et al. 2017, 2021; Naidu et al. 2020). If so, the DART impact, which causes ejecta particles to fall onto this body's surface, may provide a unique situation that disturbs its surface. If the kinetic energy delivered to it is high, its shape configuration may change, enhanced by rotation. This section summarizes recent efforts in quantifying Didymos's effective gravity field, its structural conditions and reshaping mechanisms, the surface response to DART impact-driven ejecta falling, the probability of ejecta collisions with Didymos, and an approach to measuring the magnitude of Didymos's reshaping.

2.2.1. Correlations between Gravity Fields and Material Distributions

This section discusses how Didymos's surrounding dynamic environment depends on its internal structure. We apply a mass-concentration (mass-con) model that discretizes the mass distribution into a set of many small point masses (Soldini et al. 2020). The model accounts for the gravity field surrounding Didymos by considering $T_{\rm sp} = 2.26$ hr and a constant volume of 2.54×10^8 m^3 with different bulk densities. The following analyses only focus on the vicinity of Didymos, in which Dimorphos's gravity is assumed to be negligible.

Zero-velocity curves describe the orbital energy level of small objects within a considered system. They provide qualitative information about the bounded particle dynamics under energy limits. Equation (1) defines a potential, denoted as Ω, that accounts for both gravitational and centrifugal effects in the frame fixed at Didymos (Murrary & Dermott 2000),

$$\Omega = -\frac{1}{2}\omega_{\rm sp}^2(x^2 + y^2) + U_g, \tag{1}$$

where $U_g < 0$ is the gravitational potential, and $\omega_{\rm sp}$ is the spin rate. Using the mass-con model yields

$$U_g = -\sum_{i=1}^{N} \frac{Gm_i}{r_{ik}}, \tag{2}$$

where G is the gravitational constant, m_i is the ith point mass within the set of N particles characterizing Didymos's mass distribution, and r_{ik} is the distance between the ith particle and a considered location. In the rotating frame, the x-axis corresponds to the longest principal axis, the y-axis is along the intermediate axis, and the z-axis is along the shortest axis, which also corresponds to the spin axis. The Ω may possess local maxima or saddle points, depending on $\omega_{\rm sp}$. These points are the so-called dynamic equilibria, where the net acceleration becomes zero. The Ω level exhibits energy ridges crossing these equilibria and surrounding the dynamic environment (Murrary & Dermott 2000). Inside the ridges, a particle's motion is bounded, given Ω. On the other hand, if particles are outside the ridges, the motion is unbounded.

Figure 2 shows the zero-velocity curves surrounding Didymos on its equatorial plane; each contour shows the same Ω level. Figure 2(a) depicts the case of $\rho_B = 1820$ kg m^{-3}. A lower bulk density than the nominal case, i.e., $\rho_B = 2170$ kg m^{-3}, results in lower gravity acceleration, while the rotational acceleration remains unchanged. This leads to a dominant rotational effect in the surrounding area and so no existence of equilibria. Figure 2(b) gives the case of the nominal bulk density, which is

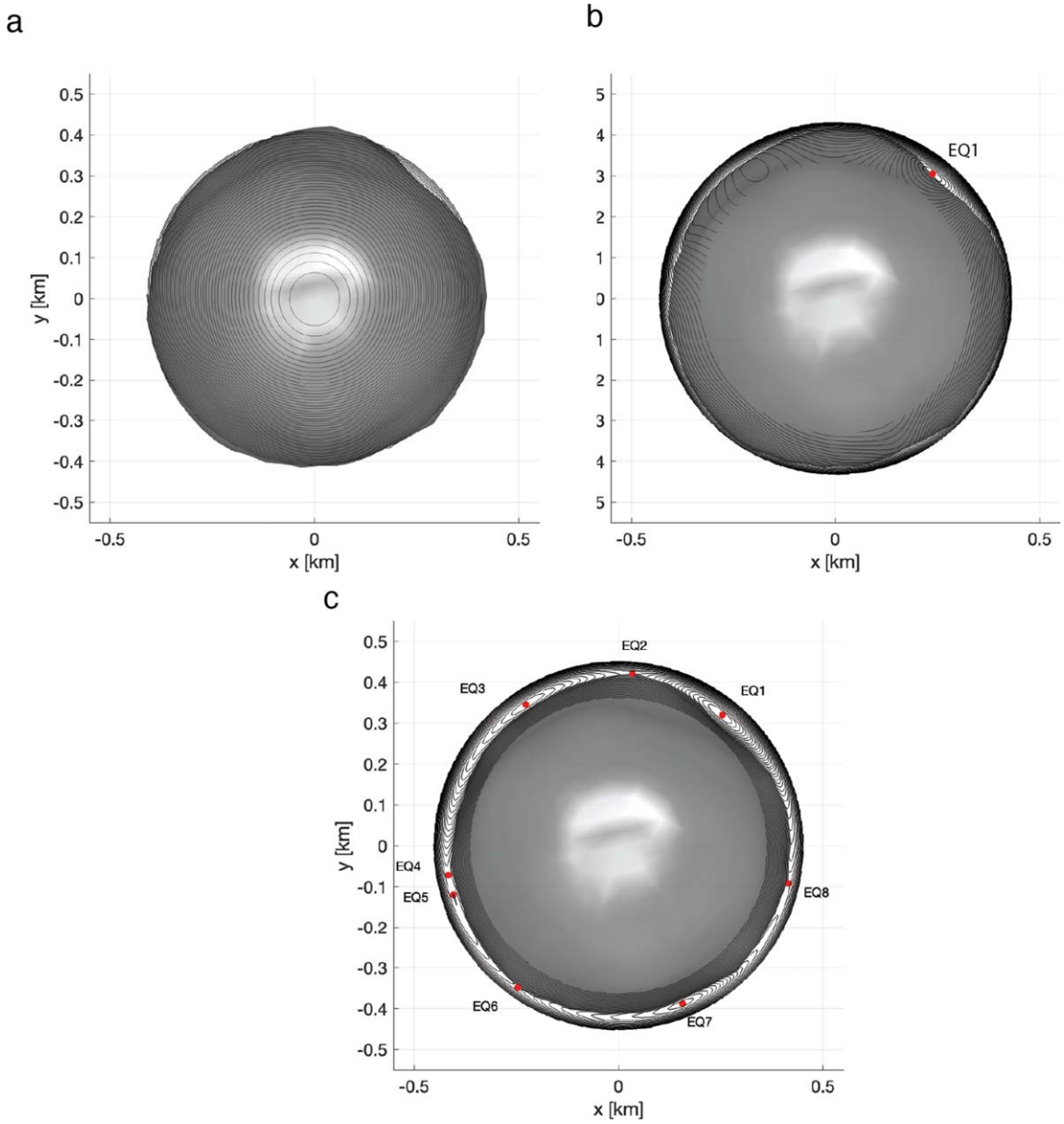


Figure 2. Zero-velocity curves on the equatorial plane with three bulk densities. (a) $\rho_B = 1820$ kg m^{-3}. (b) $\rho_B = 2170$ kg m^{-3}. (c) $\rho_B = 2520$ kg m^{-3}. The red points indicate the equilibrium points, where net acceleration in the rotating frame becomes zero, and the contours show the zero-velocity curves. Each equilibrium point is labeled as EQ. The three bulk density cases are tested based on the recent radar-based measurements, 2170 ± 350 kg m^{-3} (Naidu et al. 2020).

$\rho_B = 2170$ kg m^{-3}. There is only one equilibrium point (EQ1), which is linearly stable and almost touches the surface at the concavity. Particles resting initially but later ejected from this region may stay there because this stable equilibrium point may keep them trapped. On the other hand, other equatorial areas do not host equilibria and are outside the energy ridges, causing material shedding and unbounded motion. If $\rho_B = 2520$ kg m^{-3}, the gravitational effect becomes higher, giving the presence of more equilibria (Figure 2(c)). Eight equilibria may surround the body for this case. Four equilibria (EQ1, EQ3, EQ5, and EQ7) are linearly stable, while the other four (EQ2, EQ4, EQ6, and EQ8) are unstable. All of the identified equilibria stay near the equatorial plane.

The results show that particles resting on the equatorial surface are generally susceptible to ejection due to a high centrifugal force. Even the nominal bulk density case gives a condition that particles may be shed if no attractive force keeps them on the surface. This finding implies that if particles are cohesionless, they cannot rest on the surface and may tend to move toward the equator, and some may depart from the surface (Yu et al. 2018). As shown below, this rotational sensitivity directly correlates with the internal structure (Section 2.2.2).

2.2.2. Present Structural Condition

This section examines Didymos's current structural condition by applying a semianalytical approach (Nakano & Hirabayashi 2020). The parameter used here is the critical cohesive strength, $C_{\rm crit}$, which defines the minimum cohesive strength that the body must possess to remain structurally intact (Hirabayashi 2015). If a structural element has an actual cohesive strength lower than $C_{\rm crit}$, it should fail structurally and experience inelastic deformation. Depending on where and

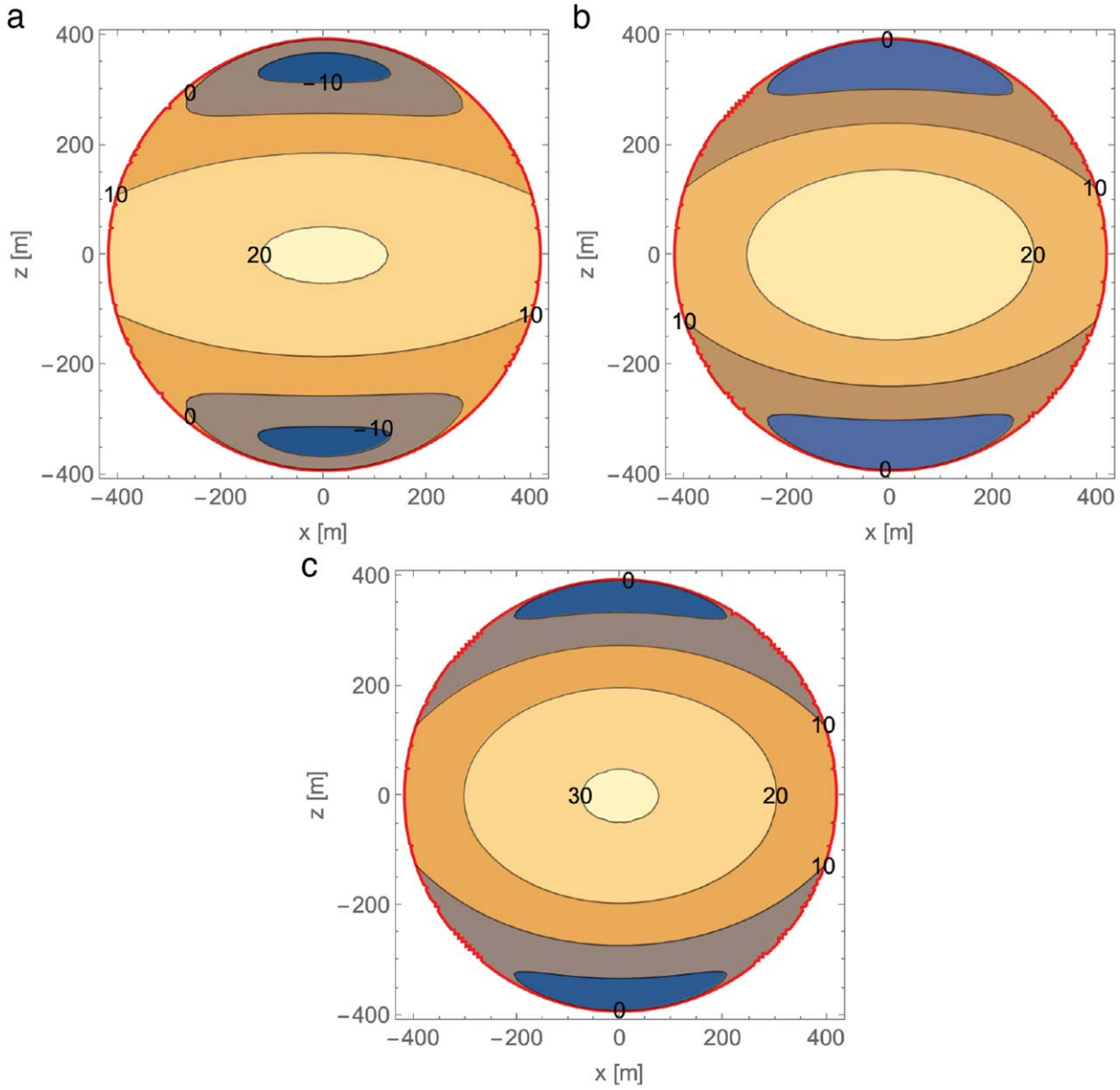


Figure 3. Spatial distributions of critical cohesive strength, $C_{\rm crit}$, with different bulk densities (the contours show its magnitude). If $C_{\rm crit}$ is positive, an element within the body should have cohesive strength; otherwise, that region should mechanically fail. The angle of internal friction, θ, is 35°. (a) $\rho_B = 1820\,{\rm kg\,m^{-3}}$. (b) $\rho_B = 2170\,{\rm kg\,m^{-3}}$. (c) $\rho_B = 2520\,{\rm kg\,m^{-3}}$. For all cases, the shape considered has dimensions of 837 m × 832 m × 786 m. The used dimensions lead to an ∼10% variation in volume, although this discrepancy does not affect the final results. Similar to Figure 2, the three bulk density cases are tested here based on the recent radar-based measurements, $2170 \pm 350\,{\rm kg\,m^{-3}}$ (Naidu et al. 2020).

how this condition appears, the magnitude of reshaping varies (Hirabayashi 2015). Details are provided in Section 2.2.3.

The semianalytical approach yields the spatial distributions of $C_{\rm crit}$ within Didymos. Assuming that the density distribution is uniform, this approach calculates the stress distributions by solving the equilibrium stress equation with the traction boundary conditions (Nakano & Hirabayashi 2020). The computed stress distributions are then applied to the Drucker–Prager yield criterion (Chen & Han 2007) to determine $C_{\rm crit}$ at a given location. The angle of internal friction, θ, is fixed at 35°, based on a study reporting the properties of terrestrial materials (Lambe & Whitman 1969).

This approach is applied to compute $C_{\rm crit}$ for Didymos at $T_{\rm sp} = 2.26$ hr. The asteroid is assumed to be a uniformly rotating triaxial ellipsoid with dimensions of 837 m × 832 m × 786 m based on the Design Reference Asteroid (DRA) v3.03A parameters available through the DART Science Operations Center site.[13] Figure 3 illustrates the spatial distribution of $C_{\rm crit}$ on the asteroid's cross section with the three bulk densities discussed in Section 2.2.1, i.e., 1820, 2170, and 2520 $\rm kg\,m^{-3}$. The $C_{\rm crit}$ is always positive in the interior and on the surface at lower altitudes for all bulk densities. This outcome suggests that cohesionless materials cannot support the current structure. When inelastic deformation spreads over these regions, the body cannot support its shape and eventually experiences a complete breakup (Zhang et al. 2017, 2021). However, this breakup scenario contradicts the current configuration (i.e., the body exists without failure), meaning that this body

[13] The available dimensions are 832 m × 837 m × 786 m and derived by Naidu et al. (2020); we reorder the axes to avoid numerical issues in the semianalytical model that uses elliptic integrals to compute the stress field.

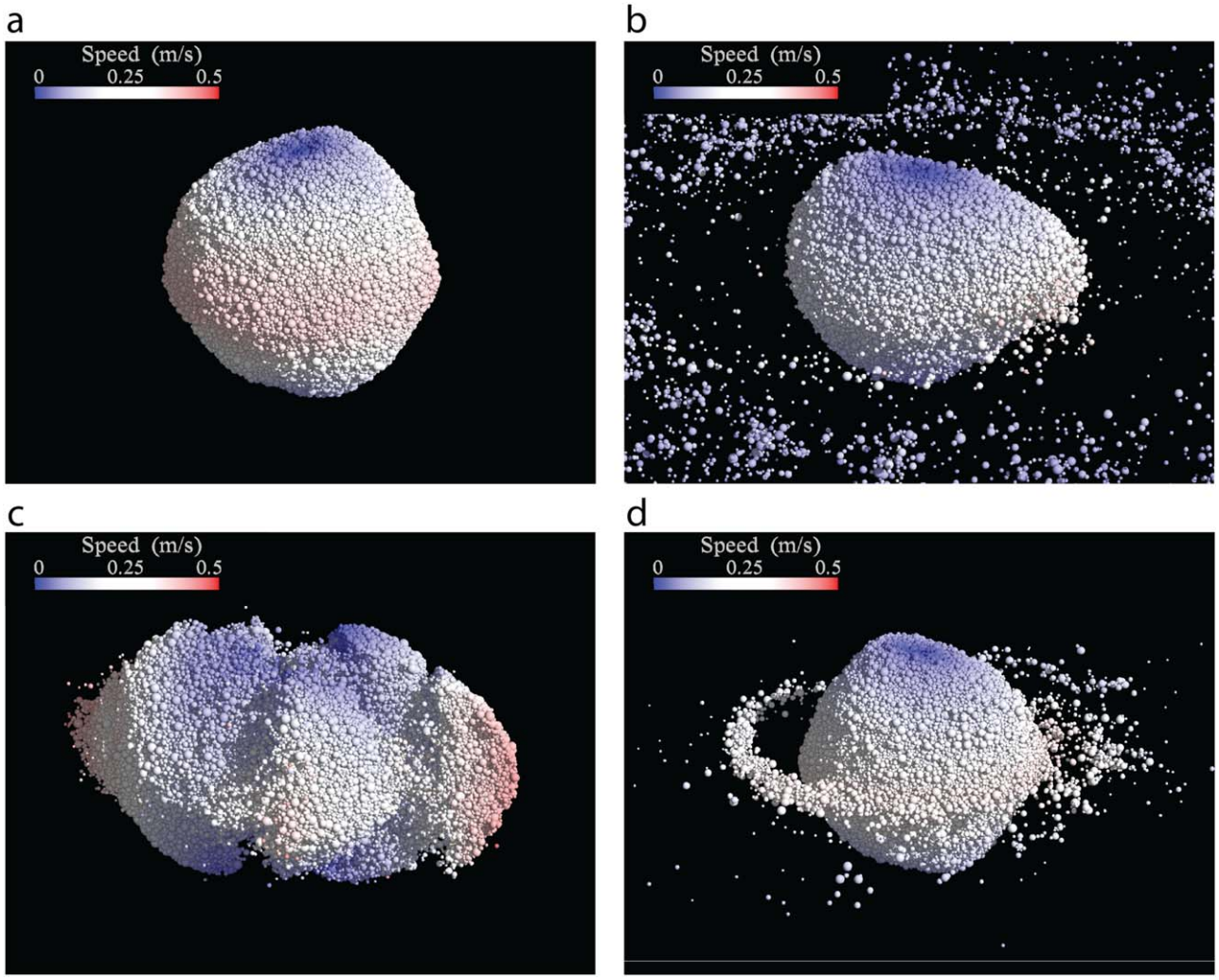


Figure 4. The pkdgrav simulations showing Didymos's reshaping modes depending on the interparticle cohesive strength, c, and the bulk density, ρ_B. The particle size distribution ranges between ∼4 and ∼16 m. The color shows the particle speed. (a) Original shape configuration. (b) $c = 320$ Pa and $\rho_B = 2170$ kg m^{-3}. (c) $c = 700$ Pa and $\rho_B = 1820$ kg m^{-3}. (d) $c = 150$ Pa and $\rho_B = 2520$ kg m^{-3}.

should have bulk cohesive strength (Zhang et al. 2017; Naidu et al. 2020).

While $C_{\rm crit}$ varies with ρ_B, the distribution trends remain unchanged. In other words, the inside always has the highest necessary cohesive strength, while the surface regions have a lower necessary cohesive strength. At the pole, on the other hand, major areas have negative stress distributions, meaning that no cohesive strength is necessary to keep these regions structurally intact. The $C_{\rm crit}$ within the considered bulk density range, $\rho_B = 2170 \pm 350$ kg m^{-3}, is about 20–30 Pa. If the actual cohesive strength is lower than that value at the central regions of this body, the body should fail structurally.

2.2.3. Reshaping Mechanisms

Sections 2.2.1 and 2.2.2 suggest that Didymos needs mechanical strength. This interpretation is consistent with earlier work (Zhang et al. 2017; Naidu et al. 2020), though a low-strength structure may be suitable for rubble-pile bodies given their formation and evolution associated with collision and reaccumulation (Michel et al. 2001, 2020; Richardson et al. 2002). The next key question is how Didymos reshapes if the body does not support the current configuration any longer. This section provides an overview of Didymos's reshaping modes at $T_{\rm sp} = 2.26$ hr, given different interior conditions, by employing two discrete element modeling (DEM) tools: pkdgrav (Schwartz et al. 2012; Zhang et al. 2017, 2021) and GRAINS (Ferrari et al. 2017, 2020). A key finding is consistent with earlier work showing that the reshaping mode driven by rotation strongly depends on the cohesive strength, density distribution, and particle arrangement and size distribution (Hirabayashi 2015; Zhang et al. 2021).

If the internal structure is homogeneous, and the van der Waals force is the primary source of cohesion (Scheeres et al. 2010), boulders and gravels require substantial interstitial fine grains to bridge with similarly sized particles and stabilize the rubble-pile structure (Sánchez & Scheeres 2014). Simulations by the pkdgrav code suggest that the critical cohesive strength, $C_{\rm crit}$, of a homogeneous Didymos-like structure with $\rho_B = 2170$ kg m^{-3} ranges from ∼11 to ∼17 Pa (Zhang et al. 2021), consistent with values provided by the semianalytical model above (Section 2.2.2) and a finite element model (FEM) study that predicted ∼20 Pa (Naidu et al. 2020). This cohesion level implies that Didymos needs grains with sizes smaller than 10 μm (Sánchez & Scheeres 2014). Figure 4 shows pkdgrav simulations that describe reshaping modes with randomly

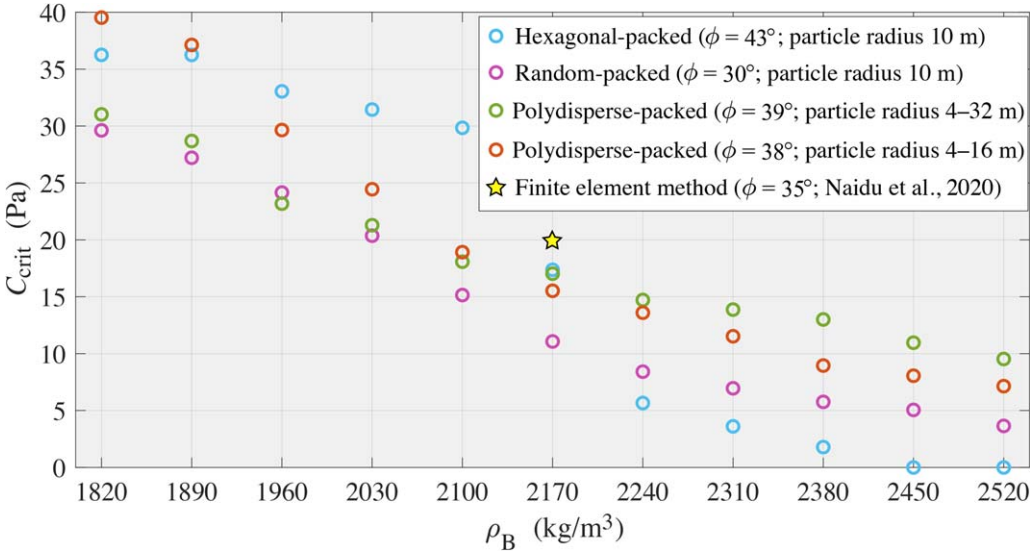


Figure 5. Critical cohesive strength C_{crit} with respect to the bulk density ρ_B for four homogeneous rubble-pile structures. This figure is an updated version of Figure 12 of Zhang et al. (2021), including the results from the FEM model by Naidu et al. (2020) and excluding all but the C_{crit} values.

distributed particles (∼4–16 m in diameter). The same bulk densities as before, $\rho_B = 1820$, 2170, and 2520 kg m^{-3}, are considered.

When $\rho_B = 2170$ kg m^{-3}, the interparticle cohesive strength, c, should be higher than 330 Pa to maintain global structural stability. If c is less than that, the internal and surface regions fail almost simultaneously. Figure 4(b) shows the reshaping mode when $c = 320$ Pa. The resulting reshaping process yields a pancake-like shape. When $\rho_B = 1820$ kg m^{-3}, the structure needs $c = 710$ Pa to maintain its global stability; otherwise, it would be unstable (Figure 4(c)). The resulting reshaping process is a breakup because the internal structure is most sensitive to structural failure at this rapid spin state (Section 2.2.2), and the large interparticle cohesive strength makes the body brittle and able to break easily after the internal structure fails. The split components are relatively large because of the cohesive strength still connecting the particles while global fractures propagate through the global shape. If $\rho_B =$ 2520 kg m^{-3}, the c value should be higher than 160 Pa to avoid reshaping. If $c = 150$ Pa (Figure 4(d)), the reshaping mode mainly consists of surface material movements.

Figure 5 illustrates `pkdgrav` simulations exploring a larger parameter space (Zhang et al. 2021). The results show that if ρ_B increases, C_{crit} becomes lower. This behavior stems from the increase in the gravitational attraction, leading to a more structurally stable configuration. The lower-density case ($\rho_B <$ ∼2170 kg m^{-3}) leads to tensile failure, while the higher-density case ($\rho_B \geqslant$ ∼2170 kg m^{-3}) results in surface shedding and internal deformation (Zhang et al. 2021). Furthermore, the internal structure variations change C_{crit} up to 30%. The slope of the C_{crit} variation for a hexagonally packed configuration is higher than that for polydisperse cases. A well-organized structure like a hexagonally packed configuration may be more fragile when the tensile stress becomes dominant while supporting its structure under a stronger gravitational influence without cohesive strength. On the other hand, the polydisperse configuration needs a lower cohesive strength than the hexagonal packing configuration when the bulk density is low.

Recent in situ observations of top-shaped asteroids Bennu and Ryugu allowed inference of their mechanically weak surface structures (Arakawa et al. 2020; Scheeres et al. 2020; Roberts et al. 2021). If Didymos has a similar heterogeneous structure consisting of a weaker surface layer and a relatively stronger interior, the major reshaping process is surface mass movements (Ferrari & Tanga 2022). Figure 6 illustrates simulations from the `GRAINS` code showing how the existence of a mechanically strong core changes the reshaping mode. The strong inner core represents the presence of nondeformable volume within the asteroid's internal structure and may be made of a single monolithic block or a set of multiple large blocks.

If the volumetric ratio of the strong core to the entire body, ψ_c, is about 50%, and $\rho_B = 2170$ kg m^{-3} (Figure 6(a)), the reshaping mode consists of the formation of a small ring close to the equator with approximately 3.6% of Didymos's total mass. If $\psi_c = 25\%$ and $\rho_B = 2170$ kg m^{-3} (Figure 6(b)), the asteroid deforms to enhance its equatorial ridge. A smaller strong core causes Didymos to experience large reshaping and mass loss. For example, if $\psi_c = 10\%$ and $\rho_B = 2520$ kg m^{-3}, the reshaping mode is significant, leading to substantial mass ejection from the equator (Figures 6(c) and (d)). When a uniform density body consists of a mechanically weak surface layer and a strong core, mass ejection may reach only 1.2% of the total mass (Figure 6(c)). On the other hand, when the asteroid has a denser inner core with a density of 4236 kg m^{-3} and an underdense surface layer with a density of 502 kg m^{-3} and a low mechanical strength, mass ejection may reach about 18% of the total mass (Figure 6(d)).

These results show that a higher ψ_c prevents global deformation but allows surface material movements, causing exposure of mechanically strong areas at the poles. For a very high ψ_c value, particularly larger than 50%, the global shape can remain almost intact, even when the external layer is made of loosely bonded materials, because of low cohesion and shear driven by friction between irregularly shaped particles (Ferrari & Tanga 2022). Otherwise, the resulting mass movements on the surface enhance the equatorial ridge. This finding is consistent with conclusions made by earlier numerical and theoretical analysis (Hirabayashi 2015; Hirabayashi et al. 2015; Zhang et al. 2017).

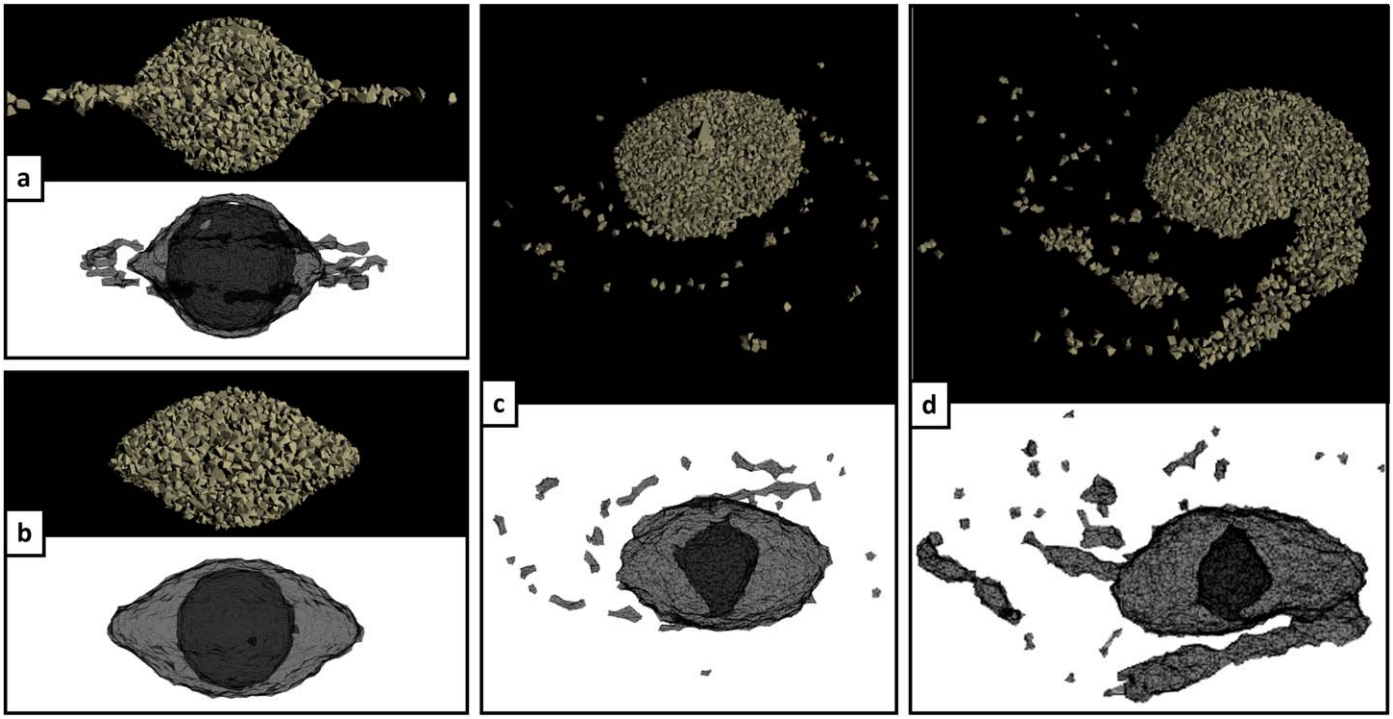


Figure 6. GRAINS simulations showing Didymos's reshaping modes as a function of the bulk density, ρ_B, and the volumetric ratio, ψ_c. The mass ejection ratio, M_e, is the ratio of the ejected mass to the total mass. The particle diameter is on the order of ∼10 m. For each panel, the upper figure is the external view, while the lower figure illustrates the inner structure with a dark region identifying the inner stronger core surrounded by a transparent layer of fragmented material. (a) $\psi_c = 50\%$ and $\rho_B = 2170\ \mathrm{kg\ m^{-3}}$, leading to $M_e = 3.6\%$. (b) $\psi_c = 25\%$ and $\rho_B = 2170\ \mathrm{kg\ m^{-3}}$, leading to $M_e = 0.04\%$. (c) $\psi_c = 10\%$ and $\rho_B = 2520\ \mathrm{kg\ m^{-3}}$, leading to $M_e = 1.2\%$. (d) $\psi_c = 10\%$ and $\rho_B = 2520\ \mathrm{kg\ m^{-3}}$, leading to $M_e = 18\%$. The difference between panels (c) and (d) is that while panel (c) considers a uniform density distribution, panel (d) describes a case with a core density of $4236\ \mathrm{kg\ m^{-3}}$ and an underdense surface density of $502\ \mathrm{kg\ m^{-3}}$.

2.2.4. Reshaping after the DART Impact

The DART impact creates particle ejection flying at various speeds. For the nominal case, while fast particles in the ejecta plume escape from the Didymos system, some low-speed particles may return to Dimorphos or hit Didymos. This section discusses how such slow particle collisions influence the surface conditions on Didymos.

Impact simulations were carried out using the GDC-i code, a soft-sphere DEM code for simulating impacts at various velocities (Sánchez Lana & Scheeres 2018). This simulation tool considers granular beds in a container to mimic Didymos's surface environment at different latitudes, assuming that the body shape is spherical. The granular bed is 1 m × 1 m × 0.8 m in size and consists of 60,000 spherical particles. The particle diameter distribution ranges between 1 and 3 cm, and the grain density, ρ_G, is $3400\ \mathrm{kg\ m^{-3}}$. The test-bed structure has a porosity of $\phi_0 = 36\%$–37%. Also, the angle of internal friction, θ, is set to be ∼35°. Particles at the bottom of the container are kept motionless, and the container has periodic boundary conditions in the horizontal direction. The gravitational acceleration is set to the Didymos value of $2.32 \times 10^{-4}\ \mathrm{m\ s^{-2}}$. The bulk cohesive strength, C_0, is initially 25 Pa everywhere and then lowers to 0 Pa in the region affected by the collisions. The projectiles, i.e., ejecta particles coming from the DART impact site, are spheres with a diameter of 10 cm and the same internal density as the surface particles ($\rho_G = 3400\ \mathrm{kg\ m^{-3}}$), leading to a mass of $M_{\mathrm{ejc}} =$ 1.78 kg. Though applying a different bulk cohesive strength, each experiment uses the same granular bed, shoots the same impactors five times at an interval of 2 s with the same impact speed, and continues with no further impacts for 290 s (Figure 7).

Figure 8 shows the average speed of surface particles in the horizontal plane, V_x, 12 s after a shot of the last projectile for two impact speeds: $V_{\mathrm{ejc}} = 1\ \mathrm{m\ s^{-1}}$, an upper limit of the impact speed of ejecta on Didymos if there are no fast ejecta approaching it (Yu & Michel 2018), and $V_{\mathrm{ejc}} = 5\ \mathrm{m\ s^{-1}}$. The results show that for $C_0 > 25$ Pa, mass movements on a large scale are unlikely to occur, even for five successive impacts. There is no significant particle movement ($\sim\mathrm{mm\ s^{-1}}$) below the top surface (about the 0.8 m line), whereas particles above the surface have acquired speeds an order of magnitude smaller than the impact speed. These simulations lead to the conclusion that a surface condition with $C_0 \geqslant 25$ Pa and $V_{\mathrm{ejc}} \leqslant 5\ \mathrm{m\ s^{-1}}$ is enough to avoid disturbance on Didymos's surface. However, our numerical experiments suggest that if $C_0 < 5$ Pa, which is comparable to C_{crit} at middle and high latitudes, impact-induced mass movements may happen for $V_{\mathrm{ejc}} \geqslant 1\ \mathrm{m\ s^{-1}}$.

2.2.5. Influence of Ejecta Speed and Cone Geometry on Ejecta Particle Collisions with Didymos

The remaining issue is whether the DART-driven ejecta reach Didymos. Earlier work revealed that many ejecta particles at speeds of less than the escape velocity[14] ($\sim 0.43\ \mathrm{m\ s^{-1}}$) hit Didymos after orbiting the system for a while (Yu et al. 2017; Yu & Michel 2018). On the other hand, whether the collisions of fast ejecta occur on Didymos remains unresolved. In the nominal impact scenario, in which the DART spacecraft hits Dimorphos's surface almost normally,

[14] The escape speed is calculated assuming that a particle is sitting on Didymos's surface.

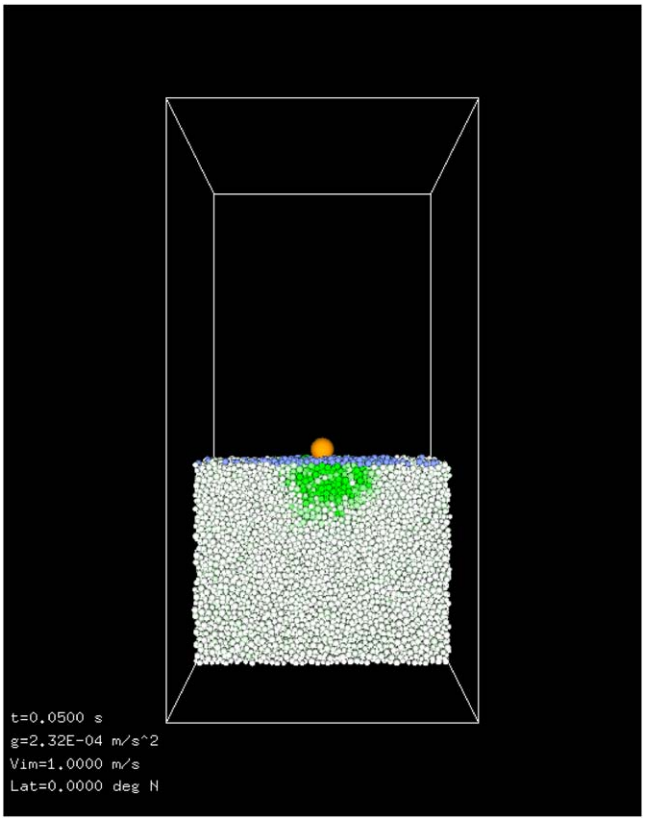


Figure 7. Simulation setup. The image shows a perpendicular impact at 1 m s^{-1} on a cohesive bed. The color green is linked to particles affected by the contact process.

the ejecta cone does not cross Didymos (Yu et al. 2017; Yu & Michel 2018). However, given limited information on the topographic condition at the impact site, an oblique impact scenario is also possible to create different cone geometries from the nominal case, some of which may cross Didymos. This section applies a simple statistical model to investigate the probability that fast ejecta (>0.8 m s^{-1}) directly approach this asteroid without orbital revolution under the surface slope uncertainty.

The model first determines the DART spacecraft condition and the locations and orientations of Didymos and Dimorphos at the impact event by using the DART SPICE kernels (Design Reference Mission v3.00) via the JPL/NAIF SPICE tool (Acton 1996; Anton et al. 2018). The script is written in Python and uses SpiceyPy for the SPICE toolkit (Annex et al. 2020). Given the SPICE kernels, the expected impact time is 23:14:18 on 2022 September 26 UTC. The impact out-of-plane angle is ~9°.62, and the impact speed is 6.14 km s^{-1}, although these values are subject to change. The ejecta generation and cone geometry for this event were computed using the scaling relationship approach developed by Richardson et al. (2007; also see a summary of their techniques in the Appendix). The ejection speed from the impact site constrains the estimated arrival time of the ejecta at Didymos and the asteroid's orientation at that time. For simplicity, the model does not track the locations of particle landing but computes its closest distance from the center of mass of Didymos based on the two-body problem concept, where Didymos is assumed to be a spherical body. The particle's closest distance from the center of mass is then compared with the Didymos radar-driven shape model. If this point is within this asteroid's surface geometry, we consider that the particle hits Didymos. Because our approach focuses on particles flying faster than the escape speed, this two-body problem approach is an appropriate approximation to describe their trajectories. Each run generates the ejecta cone geometry by computing particle trajectories with a 4° azimuth interval. If the collision event happens, it records the event; otherwise, it moves on to the next run without recording.

A total of 15,000 test runs were performed to find the statistical trends of the collision events. We used two uniformly random variables (decl. and R.A.) to compute the surface normal at the DART impact site on Dimorphos. To determine the updated surface for each test run, the model first defines the original surface normal. This original surface normal is then updated by adding the random variables; the decl. variation from the original surface normal, later denoted as the deviation angle, is limited to be no larger than 45°. In addition to the variations in the surface normal, we consider how the timing of ejection and the surface strength, which mainly control the ejection speed, affect the probability of the collision events. Three cases were considered. The first two cases represent when the impact condition is in the gravity regime with zero cohesion and have different timings of ejection. The first case assumes a timing of 5 s, which generates ejecta with an ejection speed of ~0.8 m s^{-1}, while the second case considers that of 0.1 s, which is equivalent to ~14 m s^{-1}. These cases represent relatively early stages of the crater formation, which may continue for about 760 s.[15] The last case is when the DART impact occurs on a surface with a cohesive strength of 2000 Pa[16] and the timing of ejection considered is 0.1 s, which is equivalent to an ejection speed of 14 m s^{-1}. The crater formation timescale for this case is about 16 s.

Each case is carried out for 5000 test runs. In the first case, 386 runs were identified to encounter collisions, leading to a collision probability of ~7.7%. The second case, on the other hand, had 660 collision events (~13.2%). The discrepancy of these cases results from the ejecta speed, which determines how long the ejecta need to travel to arrive at Didymos. Fast ejecta with a speed of ~14 m s^{-1} only take 1.5 minutes to arrive at the asteroid. Within this timescale, the contribution of Dimorphos's velocity to the ejecta motion does not affect the final destination much. On the other hand, slow ejecta with a speed of ~0.8 m s^{-1} arrive at Didymos ~25 minutes after the departure, and this asteroid's velocity is no longer negligible and causes a drift of the ejecta motion. Finally, given the relatively fast ejecta, the third case also had a similar 641 collision events (~12.8%).

Figure 9 shows the fractions of collision events and total cases as functions of the deviation and impact angles. Collision events require the deviation angle to be larger than 17° (Figure 9(a)). The fraction for the 0.1 s ejection timing cases (i.e., the second and third cases) is, in general, slightly higher than that for the 5 s ejection timing case (i.e., the first case). Again, this discrepancy results from the travel time between Didymos and Dimorphos. Furthermore, impact angles between 40° and 70° can lead to collisions (Figure 9(b)). These results suggest that

[15] If the impact is subcatastrophic, the crater formation likely continues up to 2 hr (S. D. Raducan & M. Jutzi 2022, in preparation; A. M. Stickle et al. 2022, in preparation). However, we focus on a typical crater formation process.

[16] This cohesive strength was selected to discuss a high-cohesion case, leading to an end-member of cohesive scenarios.

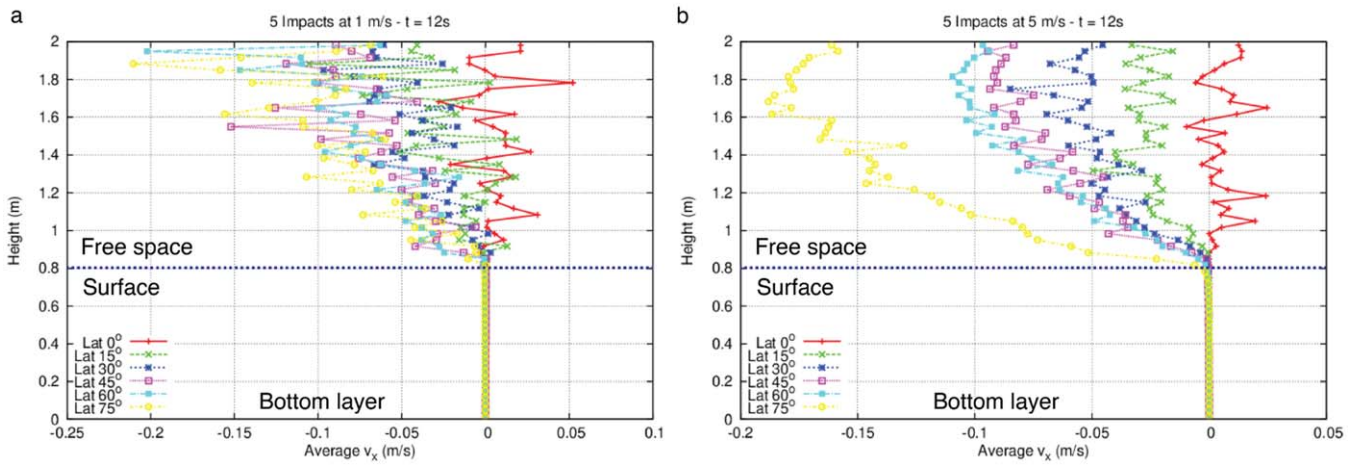


Figure 8. Velocity profile of the particles in the simulation box 12 s after the last projectile was shot. Each line corresponds to a different latitude. Here V_x is the velocity component along the horizontal direction. The bulk cohesive strength is fixed at 25 Pa. The surface layer is located about 0.8 m from the bottom, and the region above it is free space. (a) $V_{ejc} = 1\ \mathrm{m\ s^{-1}}$. (b) $V_{ejc} = 5\ \mathrm{m\ s^{-1}}$.

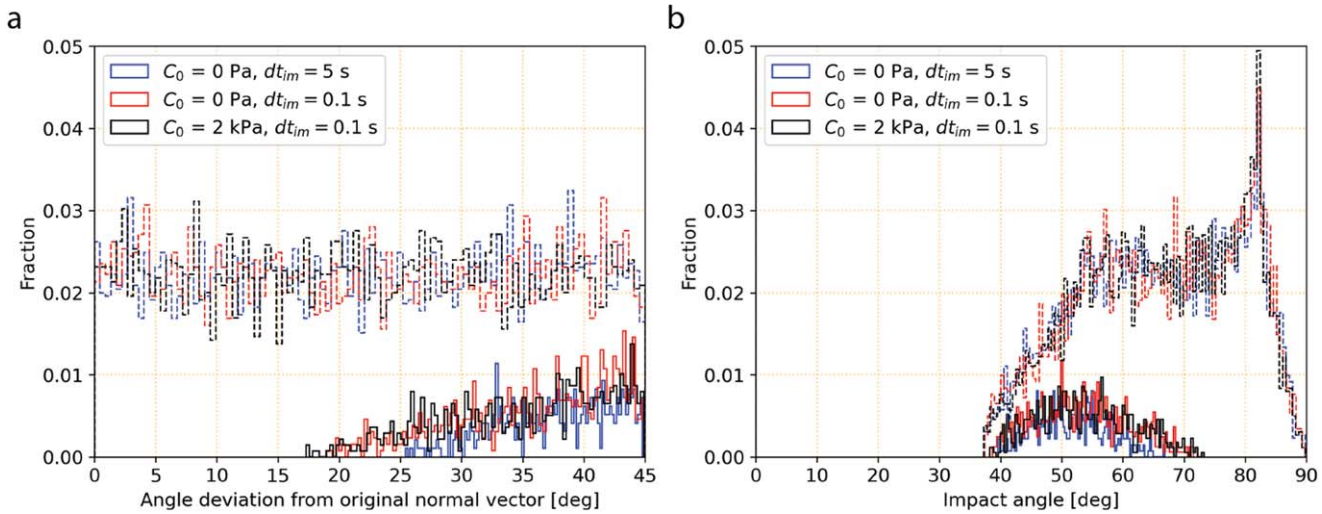


Figure 9. Fractions of collision events. (a) Collision event fraction as a function of deviation angle from the original surface normal. (b) Collision event fraction as a function of the impact angle. The solid lines denote the collision events only, while the dashed lines show the total test runs. The fractions defined here are the ratios of the number of considered events to the number of test runs.

the ejection speed ($\gtrsim 0.8\ \mathrm{m\ s^{-1}}$) and surface slope angle are the major contributors to the probability of ejecta collision events on Didymos. On the other hand, ejecta slower than $\sim 1\ \mathrm{m\ s^{-1}}$ likely hit more frequently, but such events may only occur after the particles orbit the system for a while (Yu et al. 2017; Yu & Michel 2018).

2.2.6. Measurement of Didymos's Reshaping

The reshaping timescale may be characterized by considering how quickly particles on the asteroid move, given the acceleration that they experience. The time required for a particle to move a distance q from one location to another under constant acceleration a is proportional to $(2q/a)^{0.5}$. While a varies significantly in the asteroid environment, using the acceleration at Didymos's equator, which is about $3.5 \times 10^{-5}\ \mathrm{m\ s^{-2}}$, yields an upper timescale of $\sim$1.7 hr for a particle to move $\sim$600 m, which is almost equivalent to the distance from the pole to the equator. This timescale is relatively shorter than the orbital period, 11.9 hr. Within this reshaping timescale, Dimorphos only moves 51° in orbital phase angle, and its orientation and position do not change significantly. Also, Didymos's axisymmetric shape does not enhance the angular momentum exchange. Given these conditions, the angular momentum of Didymos's rotation is assumed to remain constant during the reshaping process. Therefore, measuring Didymos's spin period change before and after the DART impact allows us to constrain its reshaping scale. Note that the ejecta falling onto Didymos and Dimorphos may also affect their spin period changes (D. C. Richardson et al. 2022, in preparation; A. Rossi et al. 2022, in preparation). For Didymos's spin, the ejecta from Dimorphos add additional angular momenta to its spin angular momentum. This process may change the asteroid's spin period up to a few seconds. However, this study does not detail this mechanism, and we leave it to future work.

As shown in Section 2.2.3, a reshaping event likely makes the body more oblate and increases its moment of inertia along the z-axis. Consequently, under a constant angular momentum, Didymos's spin period becomes longer. Figure 10 illustrates the variation in the spin period change as a function of the reshaping magnitude along the z-axis. The variation is linear with a reshaping magnitude up to 10 m, approximated as $dT_{sp} = 21.5dD$, where dT_{sp} is the spin period change in

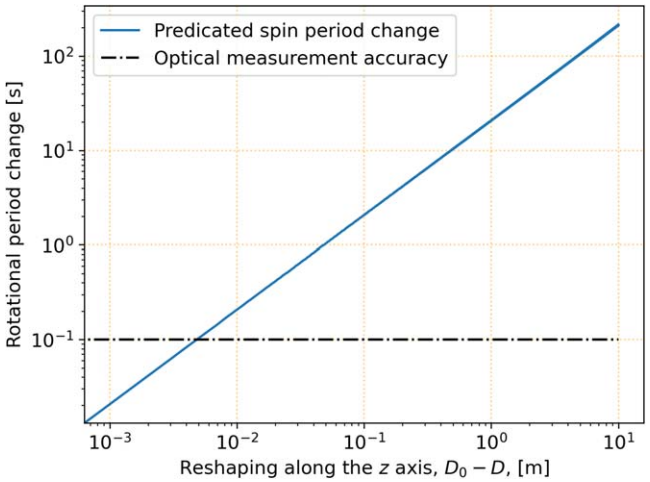


Figure 10. Didymos's reshaping-driven spin period change. The x-axis gives the reshaping-driven length change along the short axis, $dD = D_0 - D$, up to 10 m. The black dotted–dashed line is the planned optical measurement accuracy obtained by the end of 2023 April.

seconds, and dD is the z-axis length change in meters, i.e., $D_0 - D$, given the initial z-axis length, D_0, and the post-reshaping z-axis length, D (see discussions in Section 3.3 and Figure 12(b)). The asymmetric variations along the x- and y-axes do not result in significant variations in the spin period change. The predicted uncertainty of the photometric measurements for determining the spin period is less than 0.1 s by the end of 2023 April (Pravec & Scheirich 2018). With this uncertainty, telescopic observations should be able to detect a reshaping mode with deformation larger than 1 cm along the short axis (Rivkin et al. 2021).

3. Reshaping Contributions to Mutual Dynamics

3.1. Modeling the Reshaping Effects on Orbital Perturbation

The reshaping processes on Dimorphos and Didymos change the mutual gravity field, giving an additional orbital perturbation on top of the rigid-body behavior (Hirabayashi et al. 2017, 2019a). The reshaping-driven orbital perturbation may be detectable by telescopic observations, depending on the reshaping scale. R. Nakano et al. (2022, in preparation) employed a dynamics model that simulates the motion of irregularly shaped bodies under mutual gravity interactions by using an FEM to formulate mutual gravity (Yu et al. 2019). The study applies the radar shape model available from DRA and a mass of 5.2280×10^{11} kg for Didymos and a triaxial ellipsoid with a dimension of $208 \times 160 \times 133$ m^3 and a mass of 4.8417×10^9 kg for Dimorphos (Naidu et al. 2020).

R. Nakano et al. (2022, in preparation) followed the approaches by Hirabayashi et al. (2017, 2019a) to characterize the reshaping effects on orbital perturbations. The following two cases are considered. First, the normal case is when the Didymos–Dimorphos system is assumed to be in the relaxed state (Agrusa et al. 2021), and the asteroids' shapes are the original ones discussed above. Second, the alternative case is when either Dimorphos or Didymos experiences reshaping driven by the DART impact, though no DART impact-driven momentum affects the system's dynamics. As the present focus is on reshaping-driven orbital perturbation, this process effectively eliminates the contribution of the kinetic impact to the orbital perturbation (Agrusa et al. 2021; Meyer et al. 2021). Based on the discussions in Section 2.2.6, the reshaping is assumed to occur instantaneously and keep the bodies' rotational angular momenta constant during the DART impact. Specifically, the angular momentum for each component's rotation remains constant; the position and velocity of each body's center of mass remains unchanged, while the rotation varies because of the change in the moment of inertia. The orbital perturbation is assessed by subtracting the orbital motion of the normal case from that of the reshaping case.

3.2. Dimorphos's Reshaping-driven Orbit Perturbation

This section discusses orbital perturbation resulting from the DART impact-driven reshaping on Dimorphos. The analysis assumes that this asteroid's mass is unchanged because the amount of the DART impact-driven ejecta is likely negligible compared to it. For simplicity, the following steps define Dimorphos's post-DART impact shape. First, the frame rotating with Dimorphos defines the orthogonal axes, $(\xi, \eta, \zeta)^T$, along the long, intermediate, and short axes, respectively (Figure 11(a)). The ζ axis is taken to match the spin axis. The η axis points in the leading direction. The edge locations along the ξ, η, and ζ axes are $\pm\xi$, $\pm\eta$, and $\pm\zeta$, respectively. The signs describe whether the edges are placed on the positive or negative side.

The hypothetical DART impact occurs on the leading side of Dimorphos,[17] describing that the reshaping may be axisymmetric along the η axis. Modeling Dimorphos's reshaping considers the variations in the edge locations before and after the DART impact. The SPH impact simulations (Figure 1) show that the DART impact deformation mainly happens in the $+\eta$ direction (S. D. Raducan & M. Jutzi 2022, in preparation). Thus, the expected reshaping process is to make the $+\eta$ elevation lower than the original but keep the $-\eta$ elevation unchanged. The present model applies a rescaling process to the other two axes equally so that it satisfies the volume-constant condition. This reshaping process is characterized by considering the length change along the η axis, or $dL = L_0 - L$, where L_0 is the original length along the η axis, and L is the postimpact length (Figure 11(b)).

Six cases simulated by R. Nakano et al. (2022, in preparation) demonstrate orbital perturbation with dL of up to 16 m. Simulations over 180 days suggest that Dimorphos's reshaping can cause additional orbital perturbation. Figure 11(c) illustrates the relative angular position with a time interval of 6×10^4 s when the length change is 16 m. While high-frequency oscillations occur mainly due to Dimorphos's libration because the resulting orbital drift leads to an angular momentum exchange between its orbit and attitude, the observed general trend is linear growth. After 180 days, the relative angular position reaches 85°. As time proceeds, Dimorphos's reshaping causes its position to be ahead of that in the normal case, leading to a shorter orbital period.

Figure 11(d) shows the orbital period changes for the considered cases as a function of the length change along the η axis. The results indicate that the reshaping processes shorten the mutual orbital period after the DART impact. R. Nakano et al. (2022, in preparation) also found that there are limited cases for which the postimpact orbital period becomes longer.

[17] The actual DART impact will have an out-of-plane angle of ~9°.6. However, because this deviation does not significantly influence orbit perturbation (Agrusa et al. 2021), we neglect it.

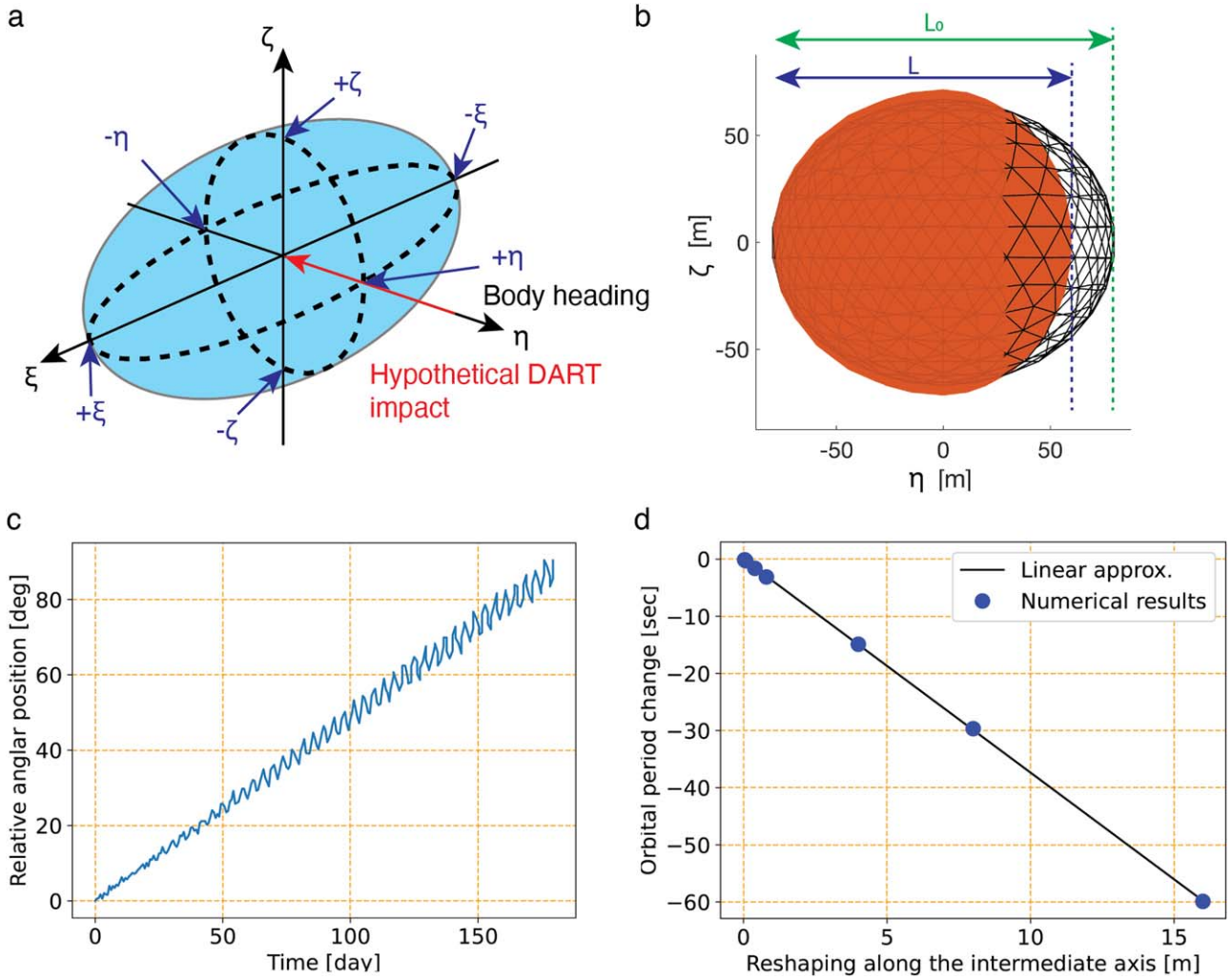


Figure 11. Dimorphos's reshaping mode and orbital perturbation. (a) Defined coordinate frame. (b) Example of reshaping. (c) Time evolution of relative angular position with a length change of 16 m. (d) Orbital period change with respect to length change.

Furthermore, the trend of the orbital period change is linear. If the axis length change is ∼2 m, the orbital period change reaches about 7.4 s, exceeding the 7.3 s measurement requirement. This magnitude may be approximately equivalent to when a 100 m diameter crater, which is similar to the crater size in the gravity regime,[18] forms after the DART impact.

3.3. Didymos's Reshaping-driven Orbit Perturbation

If Didymos's reshaping is not negligible, this process also affects the orbital perturbation. As discussed in Section 2.2.3, Didymos's fast spin may make the current axisymmetric shape more oblate if its structure reaches failure. Given the coordinate frame (x, y, z), the reshaping mode shortens the short axis, $(+z)$–$(-z)$. Similar to Section 3.2, the signs define the locations of both positive and negative edges along each axis (Figure 12(a)). The total volume remains constant, given a process equivalently rescaling along the long axis, $(+x)$–$(-x)$, and the intermediate axis, $(+y)$–$(-y)$. Later, similar to Section 2.2.6, the change in the shortest axis, i.e., $dD = D_0 - D$, is used to define the magnitude of reshaping (Figure 12(b)).

[18] We apply a π-scaling relationship (Holsapple 1993) to determine the crater size in the gravity regime with sand materials.

Ten cases from R. Nakano et al. (2022, in preparation) show the orbital perturbation for short-axis changes corresponding to ∼0.7 to ∼8 m. Figure 12(c) shows the time evolution of the relative angular position over 180 days when the short-axis change is ∼8 m. Like Dimorphos's reshaping, the relative angular position grows linearly with time. Figure 12(d) shows that the orbital period becomes shorter linearly with the reshaping magnitude. Didymos's reshaping can cause a larger orbital period change than Dimorphos's reshaping, given the same reshaping magnitude. This difference comes from the fact that Didymos plays a dominant role in controlling the gravity field. A small change in Didymos's shape induces larger variations in the mutual dynamics. Given the 7.3 s measurement requirement, if the reshaping magnitude is larger than 0.7 m, Didymos's reshaping likely influences the β value measurement. This conclusion is consistent with Hirabayashi et al. (2017, 2019a).

4. Discussions

4.1. Reshaping-driven Orbital Perturbation

This section illustrates the potential scenarios of the reshaping-driven orbital perturbation by collecting discussions in the previous sections and their unresolved issues (Figure 13). The nominal DART impact scenario only considers an addition of the

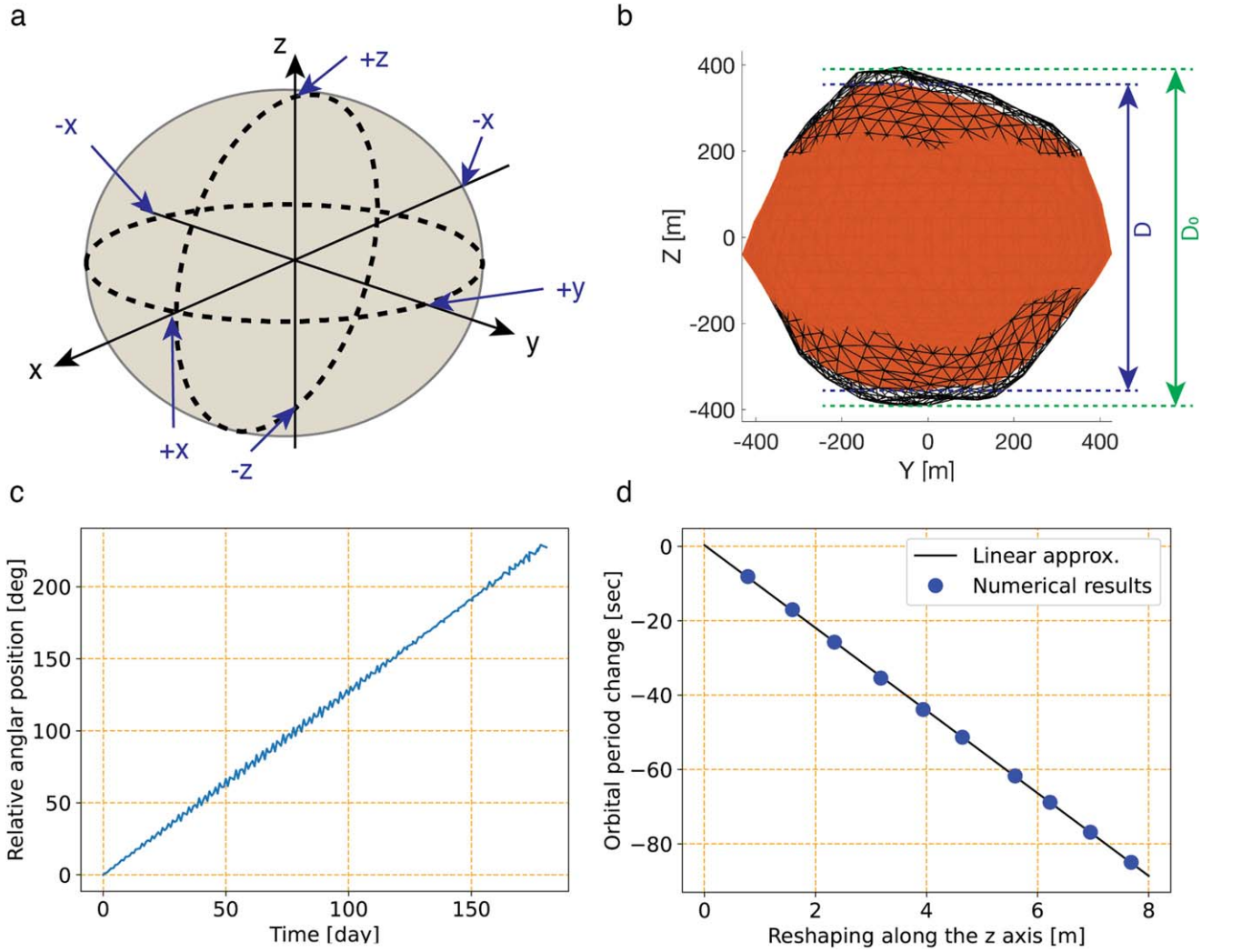


Figure 12. Didymos's reshaping mode and orbital perturbation. (a) Defined coordinate frame. (b) Example of reshaping. (c) Time evolution of relative angular position with a length change of ∼8 m. (d) Orbital period change with respect to length change.

impact-driven kinetic momentum to Dimorphos for the resulting orbital perturbation, which will be measured by using telescopic observations (Figure 13(b)). The predicted orbit period change for this case is at least ∼73 s (Rivkin et al. 2021).

However, the DART impact creates a crater on Dimorphos, and some of the resulting ejecta falls onto Didymos and may disturb its surface and interior (Figures 13(c) and (d)). While measurable reshaping processes may or may not occur on both asteroids, the major mechanisms are different (Figure 13(c)). Dimorphos's reshaping results from the cratering process. The crater size may strongly depend on the impact geometry and the surface and subsurface conditions (Section 2.1). On the other hand, Didymos's reshaping stems from its fast spin causing rotational acceleration. When the DART-driven ejecta hit Didymos's surface, the kinetic impact energy delivered by the ejecta to the surface may disturb the particles there. If the kinetic energy is high, the particles move toward the equatorial regions, making the shape more oblate.

The reshaping processes on Dimorphos and Didymos give additional orbital perturbations. Most of the considered reshaping processes push Dimorphos forward, inducing a shorter orbital period. Given the current scope of the reshaping magnitude (up to meters rather than complete disruption), the orbital period becomes linearly shorter with the reshaping magnitude. Within this range, the resulting orbit perturbation may exceed the telescopic detection limit (Rivkin et al. 2021). However, if it is much higher, the orbital period variation evolves nonlinearly and significantly (Hirabayashi et al. 2017, 2019a).

One of the critical questions is whether these asteroids indeed experience reshaping processes that may cause detectable orbital perturbation. The answer to this question depends on the current geophysical and geotechnical properties of the bodies, the DART impact on Dimorphos, and how DART impact-driven ejecta reach Didymos. The following focuses on whether the DART impact-driven reshaping is likely to occur on Dimorphos and Didymos, with limited constraints on this problem.

4.2. Dimorphos Reshaping Scenarios

Recent space exploration missions demonstrated kinetic impact experiments on small bodies and inferred that the crater formation highly depends on the surface conditions. Deep Impact's kinetic impact experiment inferred that comet Tempel 1 might possess an effective strength of up to 1–10 kPa (Richardson et al. 2007). On the other hand, the Small Carry-on Impactor (SCI) experiment on Ryugu by Hayabusa2 revealed that the impact crater formation was likely in the gravity regime

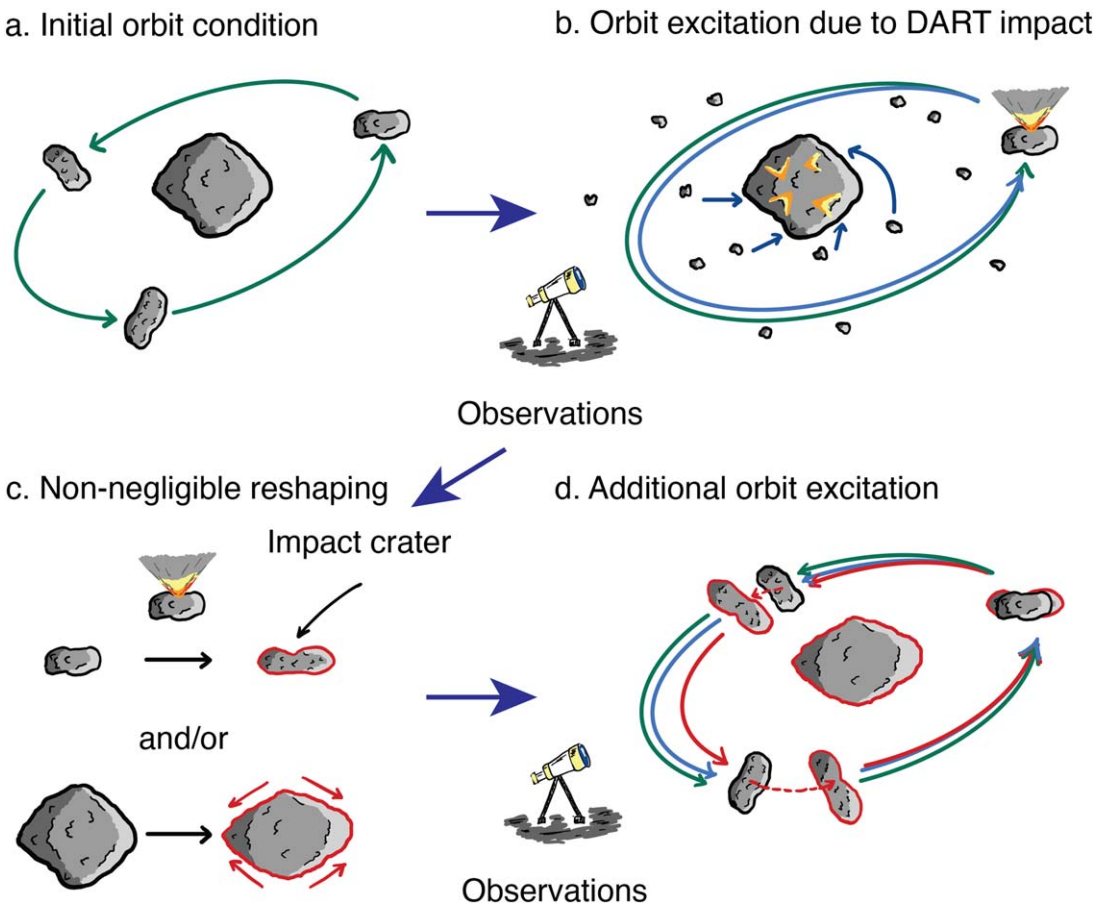


Figure 13. Reshaping-driven orbital perturbation. The green lines give the original orbit, i.e., the preimpact orbit; the blue lines show perturbed orbits driven by the DART impact without reshaping; and the red lines describe those induced by the DART impact and the reshaping process. (a) Preimpact orbit. (b) DART impact causing orbital perturbation without reshaping. (c) Nonnegligible reshaping happening to Dimorphos and Didymos. The shapes enclosed by black solid lines are the original shapes, while those enclosed by red solid lines are the deformed shapes. (d) Reshaping-driven orbital perturbation.

(Arakawa et al. 2020) for this asteroid's weak structure consisting of carbonaceous materials.

If the DART impact occurs in the gravity regime, it may result in subcatastrophic disruption. However, the Didymos–Dimorphos system's taxonomy is an Sq type (de León et al. 2006; Rivkin et al. 2021), different from the carbonaceous types identified for Bennu (B type; Lauretta et al. 2019) and Ryugu (Cb type; Sugita et al. 2019), while earlier work reported the Didymos system as an Xk type (Binzel et al. 2004).[19] The Sq-type asteroids consist of L/LL chondrite-like materials (Dunn et al. 2013). As ordinary chondrites usually have stronger mechanical strength than carbonaceous chondrites (e.g., Pohl & Britt 2020), if the target material is similar to this, the crater formation mechanism on Dimorphos should be different from that on Bennu and Ryugu. In this case, a higher fraction of the impact kinetic energy may be used to fragment target materials during the impact process (e.g., Holsapple 1993; Wiggins et al. 2019), causing the crater formation to occur in the strength regime. If there is high porosity, a large fraction of the energy may also be applied to reduce void space, which creates a smaller crater (Wünnemann et al. 2006; Collins et al. 2011). The near-surface properties are of importance for the size and morphology of the DART impact crater (i.e., Raducan et al. 2019, 2020).

[19] Some studies categorized Didymos as an Xk type in their survey studies (e.g., de León et al. 2010; Carry et al. 2016).

4.3. Didymos Reshaping Scenarios

Sections 2.2.2 and 2.2.3 outlined Didymos's structural sensitivity and its possible reshaping modes driven by fast rotation. The findings are that while rotational forces strongly contribute to the reshaping modes, they depend on the internal structure. While there may be different options, the discussions above predict that the internal structure may be mainly categorized into three types (Figure 14).

The first type is that Didymos consists of a mechanically weak, homogeneous structure but can still hold the body at the current spin period. This case may be analogous to Figure 4(b). The structure starts deforming at a longer spin period. The central and surface regions both reach their yield conditions and experience inelastic deformation. The shape continuously deforms and eventually becomes a pancake-like shape. Materials at the edges finally depart from the body, and the body eventually disintegrates into streams of small particles. A body having a weaker interior and a stronger surface may deform similarly (Sánchez & Scheeres 2018).

The second type is made of a mechanically strong, homogeneous structure. This strong structure keeps the body from structural failure and thus can spin up at a shorter spin period. However, when the spin period reaches its critical limit, the body can no longer endure high stress, failing structurally. Unlike the first type, in which moving granular elements behave like more fluidized media, the body experiences

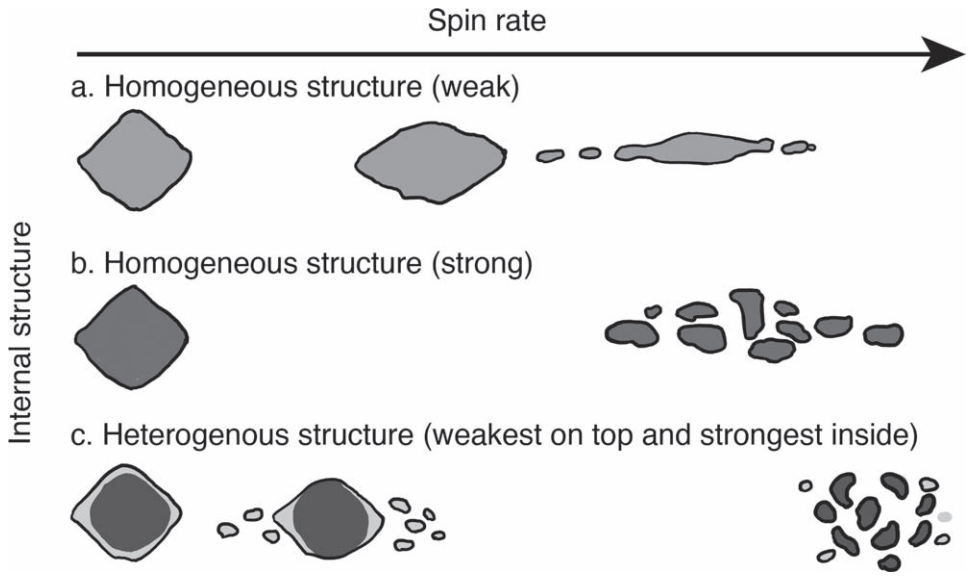


Figure 14. Potential reshaping modes of Didymos, depending on different internal structures. The horizontal axis shows the spin rate, increasing to the right. (a) Homogeneous weak structure. (b) Homogeneous strong structure. (c) Heterogeneous structure. The top layer in light gray consists of weaker structures, while the interior in dark gray is made of stronger structures. The critical spin period in which the reshaping occurs is conceptual in this schematic and depends on the existing strength.

significant fractures and falls apart into multiple pieces. This type may be similar to Figure 4(c). Related to this type, when the ridge region mechanically fails, a large chunk of that part may depart from the body to create a satellite (Jacobson & Scheeres 2011; Jacobson et al. 2016; Tardivel et al. 2018).

The third type represents a body having a weaker surface layer on top of a stronger interior. The surface layer first fails structurally at a longer spin period. As the spin period becomes shorter, surface materials move more actively toward the equatorial regions, while the interior remains intact. However, the body falls apart when the structure can no longer remain intact due to the rotational force. Given a higher internal strength, because the critical spin period may be shorter, disintegrated elements experience higher rotational forces, leading to their immediate departure from the original body. A comparable process is given in Figures 4(d) and 6. As an example, active asteroid (6478) Gault's observed mass ejection at a relatively short spin period, ∼2.5 hr, suggests that this asteroid's structure may be similar to this type (Jackson et al. 2022).

For the nominal DART impact scenario, the speed of the ejecta falling onto Didymos may be less than a few meters per second because there are few particles that reach Didymos directly (Yu et al. 2017; Yu & Michel 2018). Assuming this low-speed ejecta impact case, we discuss its influence on the reshaping. The first structural type above is a weak configuration, which can possibly result in deformation at some levels (but not large deformation). Because of its weak structure, the necessary energy level to induce deformation for this type may be lower than that for the other two types. Thus, even slow ejecta from the impact site hitting Didymos may disturb its sensitive surface. On the other hand, the second and third types may lead to a smaller reshaping process because the interior may resist such deformation. For the third type, the surface regions may be more susceptible to landslides by slower ejecta falling onto them, but the interior may still be structurally intact, keeping most of the shape configuration. Given the current structural conditions, the second and third types are more likely if the reshaping happens. Importantly, as shown in Section 2.2.6, even small reshaping processes occurring for these types may be large enough to induce measurable orbit perturbations.

4.4. Occurrence of DART-driven Reshaping Depending on Didymos's Surface Condition

At present, whether DART-driven reshaping occurs on Didymos is not well constrained. The major reason is that it is not clear how Didymos's structure currently remains intact. If van der Waals force–based cohesion is the major contributor to the body's cohesive strength, smaller particles with sizes of $\sim$10 μm must bridge and hold larger boulders. This condition implies the existence of small particles over the surface. On the other hand, if noncohesive shear effects such as interlocking play a key role in effective strength, a structure only hosting large boulders can also hold the current shape. Depending on the structure that Didymos possesses, DART-driven reshaping may or may not occur (Figure 15).

If Didymos's surface mainly consists of large boulders supported by interlocking (Figure 15(a)), a reshaping process is unlikely to occur by low-speed ejecta impacts. Such impacts do not affect the surface conditions because their kinetic energy is too low to create craters on boulders and move them (e.g., Tatsumi & Sugita 2018). If a surface layer consists of tiny particles, whether slow-speed impact events induce a reshaping process depends on the surface's mechanical strength (Figures 15(b) and (c)). A surface layer made of strongly bonded particles with a strength in excess of 5 Pa maintains its original condition without severe disturbance (Figures 15(b)). Subsequent slow-speed impacts are not sufficient to break the mechanical bonds between particles, and the surrounding area does not experience any disturbance from the impacts. However, if particles with low cohesion (less than 5 Pa) are dominant, localized disturbance may trigger a series of mass movements in larger regions (Figures 15(c)).

Further uncertainties include how the DART impact-driven ejecta approach Didymos. Ejecta dynamics simulations predict

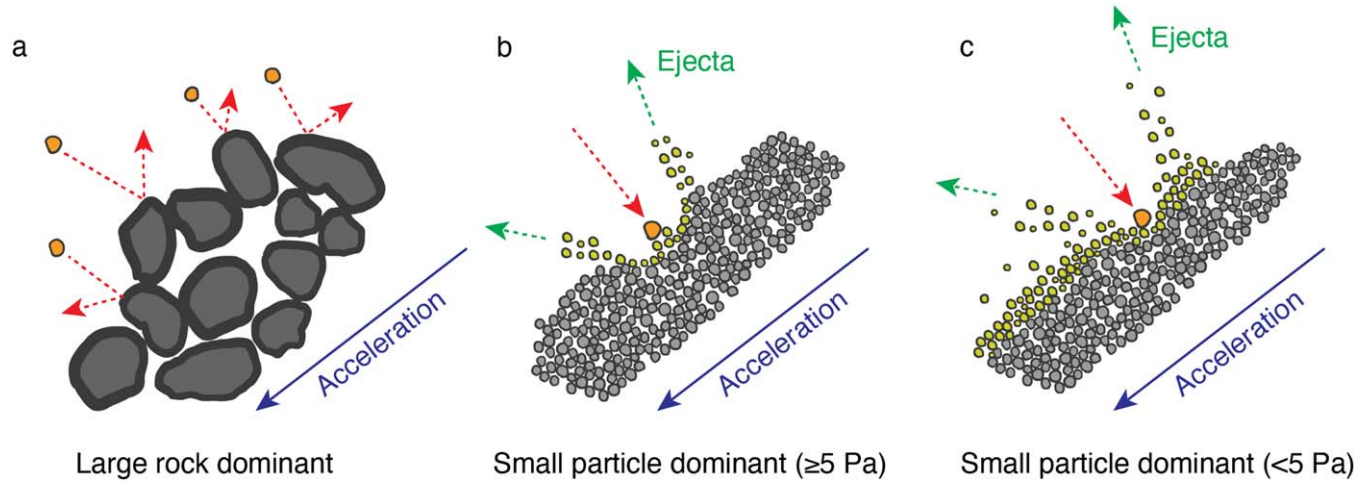


Figure 15. Low-speed particle collisions on Didymos under different surface conditions. (a) Large rocks are dominant on the surface, and low-speed collisions do not affect the conditions. (b) A surface layer with small, highly cohesive particles (⩾5 Pa) is unaffected by low-speed collisions. (c) Low-speed collisions on a small, low-cohesive surface (<5 Pa) may induce surface disturbance.

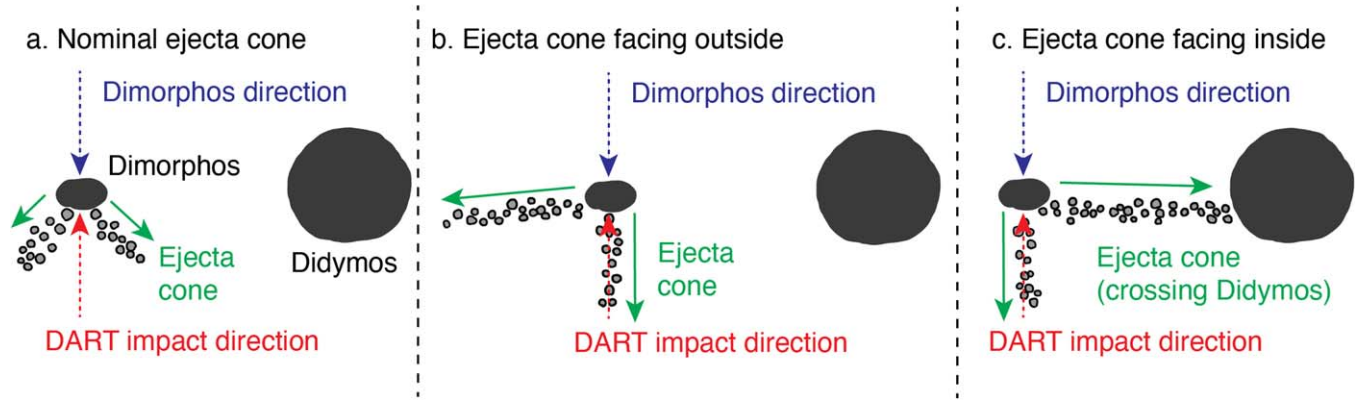


Figure 16. Variations in ejecta cone geometry driven by a sloping surface and the spacecraft shape. (a) Nominal case generating axisymmetric cone geometry. (b) Ejecta cone facing outward. (c) Ejecta cone facing inward and eventually crossing Didymos.

that if the DART impact is an ideal collision axisymmetrically generating its ejecta cone along the body's intermediate axis, the ejecta coming directly from the surface are unlikely to hit Didymos (Figure 16(a)). On the other hand, slow ejecta with speeds of less than $0.43\,\mathrm{m\,s^{-1}}$ may stay in the system, and some may fall onto Didymos due to complex force fields. However, whether this nominal case is reasonable for the DART impact is uncertain. Because limited observing capabilities prevent measuring Dimorphos's geophysical properties, the current analysis assumes Dimorphos's shape to be a triaxial ellipsoid. Observations reveal that irregular rubble-pile asteroids are common (e.g., Benner et al. 2015). Thus, the triaxial ellipsoid assumption may make the present problem too ideal. In fact, Squannit, the secondary of Moshup, is not exactly a triaxial ellipsoid (Ostro et al. 2006). Also, Hayabusa2's SCI experiment exhibited a highly asymmetric ejecta cone, suggesting a strong dependence of ejecta generation on the surface condition (Arakawa et al. 2020). If Dimorphos is indeed different from the ideal case, the ejecta cone geometry becomes complex, as an impact on a sloping surface may affect it (Figures 16(b) and (c)). If the ejecta cone faces inward and crosses Didymos, fast ejecta will hit the primary's surface, increasing the probability of a reshaping event. A variation in the surface slope up to 45° leads to an ∼13% collision probability for ejecta faster than $14\,\mathrm{m\,s^{-1}}$ in speed and an ∼8% collision probability for ejecta at $\sim 0.8\,\mathrm{m\,s^{-1}}$ in speed. Importantly, the spacecraft geometry (projectile shape) also changes the ejecta cone geometry (Raducan et al. 2022).

Because of significant uncertainties in the physical properties, it is unclear whether the reshaping occurs. However, despite the lack of assertion, such a process is unlikely to induce a collapse of Didymos's entire structure. The major reason is that if Didymos is extremely sensitive to a complete collapse and about to fail by low-speed impacts of the DART impact-driven ejecta, this body, which has experienced numerous impacts on multiple scales in the past, should not exist at present. On the other hand, a small-scale event is still possible and depends on how much ejecta hit Didymos's surface and cause a surface disturbance. This scenario is consistent with the mechanism predicted by earlier work (e.g., Cotto-Figueroa et al. 2015; Scheeres 2015; Scheeres et al. 2019, 2020), which showed the top-shape evolution under fast rotation over a long timescale. Therefore, exploring whether DART-driven reshaping may occur also informs the history of top-shaped asteroids, as well as the formation and evolution of binary asteroids. The Hera mission will provide further insights into such questions (P. Michel et al. 2022, in preparation).

5. Conclusion

This report discussed critical findings to interpret the dynamic and structural behaviors of the Didymos–Dimorphos system after the DART impact, which are enumerated below.

1. If Dimorphos consists of weak materials, and the DART impact occurs in the gravity regime, the impact process may be subcatastrophic, changing the target shape significantly. A gravity-regime impact may cause reshaping of 30 m along the impact direction on a 150 m diameter spherical body. This condition is likely the end-member of the impact process, implying that the formation of a smaller crater is more probable on Dimorphos.
2. If Didymos has the nominal bulk density, 2170 kg m^{-3}, the surface acceleration at the equator may be dominated by the rotational effect, leading to higher surface slope distributions (i.e., requiring cohesion), which is consistent with earlier findings by Naidu et al. (2020). This result suggests that granular particles cannot stay on the surface unless they experience attractive forces to stick to it. If this is not the case, they depart from the surface. This acceleration field directly correlates with the internal stress field.
3. If the observed geophysical parameters are indeed true, Didymos's structure is close to its critical condition because of the 2.26 hr spin period, which is near the spin limit. At this point, over the range of bulk density considered, 1820–2520 kg m^{-3}, most of the internal structure experiences tensile stress and thus requires mechanical strength, such as cohesive strength and geologic interlocking, to support the current configuration.
4. If some events trigger large deformation in Didymos, the resulting reshaping process may be catastrophic. Given the structural condition, the deformation process may continue until the body completely collapses. The reshaping mode strongly depends on the internal structure. A lower bulk density and a higher cohesive strength may cause a breakup into multiple large components, while a higher bulk density and a lower cohesive strength may induce surface-dominant mass movements. Furthermore, the existence of a mechanically strong core may also control the reshaping process. A large core with a limited surface layer can prevent a total collapse but enhance surface material movements.
5. If the surface structure has a cohesive strength in excess of 5 Pa, subsequent collisions of the DART-driven ejecta particles with an impact speed <5 m s^{-1} do not disturb Didymos's surface layers at all. Thus, this case does not cause further reshaping processes, keeping the structure intact. However, a surface cohesive strength of less than 5 Pa, which may be a reasonable surface condition at middle and high latitudes, may yield subsequent mass movements.
6. Without the consideration of the influence of the spacecraft's complex geometry on the ejecta cone formation, the expected DART impact geometry relative to Didymos under a surface slope uncertainty of 45° gives a 13% chance of DART-driven ejecta with speed $\gtrsim$14 m s^{-1} hitting Didymos and an 8% chance of particles with speed $\sim$0.8 m s^{-1} encountering the asteroid.
7. If a reshaping process does occur on either Didymos or Dimorphos, the resulting gravitational variation causes orbital perturbation in the mutual system. If the magnitude of reshaping is large enough, Earth-based telescopes may detect reshaping-driven orbital perturbations. If there is reshaping larger than 2 m along the intermediate axis of Dimorphos (almost equivalent to the formation of a 100 m diameter crater), the orbital period change is higher than the DART measurement requirement, which is 7.3 s. For Didymos, a reshaping larger than 0.7 m along the short axis makes the orbital period change higher than the measurement requirement. Didymos's reshaping may be measurable by tracking its spin period change. Light-curve measurements may be capable of detecting reshaping in excess of 1 cm along the short axis.

The findings above describe potential scenarios after the DART impact, though the key issue of this problem is the large uncertainties of the system's physical properties. Thus, at present, it is challenging to predict what dynamic and structural responses will actually happen after the DART impact. The scenarios strongly depend on Didymos's and Dimorphos's structural conditions, as well as how the DART-driven ejecta particles arrive at Didymos and deliver kinetic energy to induce surface disturbance. Importantly, even if the DART impact does not cause any reshaping-driven orbital perturbations, the outcomes are rich for constraining the internal structures of both of these bodies. This problem is interdisciplinary, connecting multiple physical processes, and the DART impact event offers a unique opportunity to quantify natural events happening to a binary system.

This work was supported in part by the DART mission, NASA contract No. 80MSFC20D0004 to JHU/APL. F.F. acknowledges funding from the Swiss National Science Foundation (SNSF) Ambizione grant No. 193346. R.N. acknowledges support from NASA/FINESST (NNH20ZDA001N/80MSFC20D0004). M.J., S.D.R., and P.M. acknowledge support from the European Union's Horizon 2020 research and innovation program under grant agreement No. 870377 (project NEO-MAPP). P.M. acknowledges ESA, as well as financial support from the French Space Agency CNES and the CNRS through the MITI interdisciplinary programs. E.D. and A.R. acknowledge financial support from Agenzia Spaziale Italiana (ASI; contract No. 2019-31-HH.0 CUP F84I190012600). We also thank N. L. Chabot, A. F. Cheng, A. M. Stickle, and S. Tardivel for helpful discussions that improved the quality of this manuscript.

Appendix
Ejection Speed and Ejecta Cone Geometry

This section briefly summarizes the scaling relationship approach for computing the postimpact ejection speed and angle (Richardson et al. 2007). The present model uses this approach to compute the ejection speed and angle at the DART impact site with a given surface slope, which is considered to be a statistical parameter. Table 2 lists the considered parameters. The calculation of the ejecta speed and angle starts by using the π-scaling relationship (Holsapple 1993) to calculate the crater radii in the gravity and strength regimes, R_g

and R_s, respectively. We obtain these quantities as $R_g = 45.71$ m and $R_s = 14.76$ m.

These radii and the scaling parameters yield the crater formation timescales. When the crater formation is in the gravity regime, the crater formation timescale, T_g, is given as

$$T_g = C_{Tg}\sqrt{\frac{R_g}{g}}, \tag{A1}$$

where C_{Tg} is the scaling parameter for the gravity regime, and g is the gravitational acceleration for Dimorphos. On the other hand, the timescale in the strength regime, T_s, is given as

$$T_s = C_{Ts}R_s\sqrt{\frac{\rho_t}{C_0}}, \tag{A2}$$

where C_{Ts} is the scaling parameter for the strength regime, ρ_t is the target bulk density equivalent to ρ_B,[20] and C_0 is the cohesive strength. Richardson et al. (2007) defined the effective strength $\bar{Y}$ instead of using the cohesive strength C_0. Depending on the different target conditions, C_0 may be different from Y_0; in fact, Hirabayashi et al. (2020b) argued that this is the case for larger bodies, such as the Kuiper Belt object Arrokoth. However, Dimorphos is small enough that the stress field is less than tens of Pa. Based on this, the current study assumes C_0 is comparable to $\bar{Y}$. These conditions yield $T_g \simeq 760$ s and $T_s \simeq 16$ s for $C_0 = 2$ kPa.

The model proceeds with determining the ejection speed and angle. Following Richardson et al. (2007), we compute the ideal ejection speed without the effects of gravity and friction, v_e. For the gravity-dominant regime, this quantity is given as

$$v_e = C_{vpg}\sqrt{gR_g}\left(\frac{r}{R_g}\right)^{-\frac{1}{\mu}}, \tag{A3}$$

where r is the distance from the impact point to the ejecta base on the target surface, μ is the target material parameter, and C_{vpg} is the scaling parameter given as

$$C_{vpg} = \frac{\sqrt{2}}{C_{Tg}}\frac{\mu}{1+\mu}. \tag{A4}$$

On the other hand, for the strength regime, the ideal ejection speed is given as

$$v_e = C_{vps}\sqrt{\frac{C_0}{\rho_t}}\left(\frac{r}{R_s}\right)^{-\frac{1}{\mu}}, \tag{A5}$$

where

$$C_{vps} = C_{vpg}\left(\frac{\rho_t g R_g}{C_0 + \epsilon}\right)^{\frac{1}{2}}\left(\frac{R_g}{R_s}\right)^{\frac{1}{\mu}}. \tag{A6}$$

The ϵ parameter corresponds to the Y parameter in Richardson et al. (2007), which is called the simulation stability parameter. Here we fix it at 1 Pa. The v_e value does not account for the condition that the ejection speed is affected by gravity and friction. Applying the Bernoulli principle resolves this issue by constraining the ejection speed at the largest crater radius and gives the ejection speed

$$v_{ef} = \sqrt{v_e^2 - C_{vpg}^2 gr - C_{vps}^2\frac{C_0}{\rho_t}}. \tag{A7}$$

The ejection angle, ψ_f, is formulated empirically (Richardson et al. 2007). First, the nominal ejecta angle, ψ_n, is computed as

$$\psi_n = \psi_0 - \psi_d\frac{r}{R_g}, \tag{A8}$$

where ψ_0 is the initial ejecta angle, and ψ_d is the variation. If the impact event is oblique, the ejecta angle also depends on the impact angle, $\phi_{\rm im}$, and the azimuth from the impact incoming direction, $\theta_{\rm az}$, which is given as

$$\psi_f = \psi_n - \frac{\pi\cos\phi_{\rm im}(1-\cos\theta_{\rm az})}{12}\left(1-\frac{r}{R_g}\right)^2. \tag{A9}$$

Here $\phi_{\rm im} = 90°$ represents a normal impact. Using the ejection angle finally determines the actual ejection speed:

$$v_f = v_{ef}\sin\psi_n\sqrt{1+\cot^2\psi_f}. \tag{A10}$$

There are two caveats to this approach. First, the employed approach follows the approach by Richardson et al. (2007), in which Equation (A7) uses the ejection speed without the influence of gravity and friction under the assumption that the ejection angle is 45°. This comes from the computation of C_{vpg} in Equation (A4); in this equation, the $\sqrt{2}$ factor results from the assumption of the ejection angle being 45°, i.e., $1/\sin(45°) = \sqrt{2}$. However, the ejection angle is later set to vary to compute v_f. Thus, a proper calculation may need an implicit solver to simultaneously determine v_f and ϕ_f. This process may be rather complex. Second, this scaling relationship approach assumes a flat target surface, while the DART impact site on Dimorphos is likely not so ideal. Any surface shape irregularity may change the ejection speed and ejecta cone geometry. However, numerous uncertainties regarding the geophysical and impact conditions prevent further practical analysis. This study, therefore, focuses on providing rough estimates of the ejecta conditions. Importantly, as shown in Figure 9, fast ejecta may lead to a higher probability of collision events. For this case, the ejection timescale is quite short after the DART impact, and the surface may reasonably be assumed to be flat, meaning that the derived probability for this case is meaningful. On the other hand, the slow ejecta cases may need revision because they are likely affected by complex local topographies.

[20] We use ρ_t on purpose because the bulk density is fixed at 2170 kg m^{-3} in this Appendix, unlike ρ_B.

ORCID iDs

Masatoshi Hirabayashi https://orcid.org/0000-0002-1821-5689
Fabio Ferrari https://orcid.org/0000-0001-7537-4996
Martin Jutzi https://orcid.org/0000-0002-1800-2974
Ryota Nakano https://orcid.org/0000-0002-9840-2416
Sabina D. Raducan https://orcid.org/0000-0002-7478-0148
Paul Sánchez https://orcid.org/0000-0003-3610-5480
Stefania Soldini https://orcid.org/0000-0003-3121-3845
Yun Zhang https://orcid.org/0000-0003-4045-9046
Olivier S. Barnouin https://orcid.org/0000-0002-3578-7750
Derek C. Richardson https://orcid.org/0000-0002-0054-6850
Patrick Michel https://orcid.org/0000-0002-0884-1993

Elisabetta Dotto https://orcid.org/0000-0002-9335-1656
Alessandro Rossi https://orcid.org/0000-0001-9311-2869
Andrew R. Rivkin https://orcid.org/0000-0002-9939-9976

References

Acton, C. H. 1996, P&SS, 44, 65
Agrusa, H. F., Gkolias, I., Tsiganis, K., et al. 2021, Icar, 370, 114624
Annex, A. M., Pearson, B., Seignovert, B., et al. 2020, JOSS, 5, 2050
Anton, C., Bachman, N., Semenov, B., et al. 2018, P&SS, 150, 9
Arakawa, M., Saiki, T., Wada, K., et al. 2020, Sci, 368, 67
Barnouin, O. S., Daly, M. G., Palmer, E. E., et al. 2019, NatGe, 12, 247
Becker, T. M., Howell, E. S., Nolan, M. C., et al. 2015, Icar, 248, 499
Benner, L. A. M., Busch, M. W., Giorgini, J. D., et al. 2015, in Asteroids IV, ed. P. Michel et al. (Tucson, AZ: Univ. Arizona Press), 165
Binzel, R. P., Rivkin, A. S., Stuart, J. S., et al. 2004, Icar, 170, 259
Carry, B., Solano, E., Eggl, S., et al. 2016, Icar, 238, 340
Chen, W.-F., & Han, D.-J. 2007, Plasticity for Structural Engineers (Plantation, FL: J Ross Publishing Classics)
Cheng, A. F., Michel, P., Jutzi, M., et al. 2016, P&SS, 121, 27
Cheng, A. F., Rivkin, A. S., Michel, P., et al. 2018, P&SS, 157, 104
Cheng, A. F., Stickle, A. M., Fahnestock, E. G., et al. 2020, Icar, 352, 113989
Collins, G. S., Melosh, H. J., & Ivanov, B. A. 2004, M&PS, 39, 217
Collins, G. S., Melosh, H. J., & Wünnemann, K. 2011, IJIE, 38, 434
Cotto-Figueroa, D., Statler, T. S., Richardson, D. C., et al. 2015, ApJ, 803, 25
Daly, R. T., Bierhaus, E. B., Barnouin, O. S., et al. 2020, GeoRL, 47, e89672
de León, J., Licandro, J., Duffard, R., et al. 2006, AdSpR, 37, 178
de León, J., Licandro, J., Serra-Ricart, M., et al. 2010, A&A, 517, A23
Dotto, E., Della Corte, V., Amoroso, M., et al. 2021, P&SS, 199, 105185
Dunn, T. L., Burbine, T. H., Bottke, W. F., et al. 2013, Icar, 222, 273
Ferrari, F., Lavagna, M., & Blazquez, E. 2020, MNRAS, 492, 749
Ferrari, F., & Tanga, P. 2022, Icar, 378, 114914
Ferrari, F., Tasora, A., Masarati, P., et al. 2017, Multibody System Dynamics, 39, 3
Harris, A. W., Fahnestock, E. G., & Pravec, P. 2009, Icar, 199, 310
Hergenrother, C. W., Maleszewski, C. K., Nolan, M. C., et al. 2019, NatCo, 10, 1291
Hirabayashi, M. 2015, MNRAS, 454, 2249
Hirabayashi, M., Davis, A. B., Fahnestock, E. G., et al. 2019a, AdSpR, 63, 2515
Hirabayashi, M., Nakano, R., Tatsumi, E., et al. 2020a, Icar, 352, 113946
Hirabayashi, M., Sánchez, D. P., & Scheeres, D. J. 2015, ApJ, 808, 63
Hirabayashi, M., Schwartz, S. R., Yu, Y., et al. 2017, MNRAS, 472, 1641
Hirabayashi, M., Tatsumi, E., Miyamoto, H., et al. 2019b, ApJL, 874, L10
Hirabayashi, M., Trowbridge, A. J., & Bodewits, D. 2020b, ApJL, 891, L12
Hirata, N., & Ikeya, R. 2021, Icar, 364, 114474
Holsapple, K. A. 1993, AREPS, 21, 333
Holsapple, K. A., & Housen, K. R. 2012, Icar, 221, 875
Housen, K. R., Sweet, W. J., & Holsapple, K. A. 2018, Icar, 300, 72
Jackson, P. M., Nakano, R., Kim, Y., et al. 2022, PSJ, 3, 16
Jacobson, S. A., Marzari, F., Rossi, A., & Scheeres, D. J. 2016, Icar, 277, 381
Jacobson, S. A., & Scheeres, D. J. 2011, Icar, 214, 161
Jawin, E. R., Walsh, K. J., Barnouin, O. S., et al. 2020, JGRE, 125, e06475
Jutzi, M. 2015, P&SS, 107, 3
Jutzi, M. 2019, P&SS, 177, 104695
Jutzi, M., Benz, W., & Michel, P. 2008, Icar, 198, 242
Lambe, T. W., & Whitman, R. V. 1969, Soil Mechanics (New York: Wiley)
Lauretta, D. S., DellaGuistina, D. N., Bennet, C. A., et al. 2019, Natur, 568, 55
Margot, J.-L., Pravec, P., Taylor, P., et al. 2015, in Asteroids IV, ed. P. Michel et al. (Tucson, AZ: Univ. Arizona Press), 355
Meyer, A. J., Gkolias, I., Gaitanas, M., et al. 2021, PSJ, 2, 224
Michel, P., Ballouz, R.-L., Barnouin, O. S., et al. 2020, NatCo, 11, 2655
Michel, P., Benz, W., Tanga, P., et al. 2001, Sci, 294, 1696
Murrary, C. D., & Dermott, S. F. 2000, Solar System Dynamics (Cambridge: Cambridge Univ. Press)
Naidu, S., Benner, L., Brozovic, M., et al. 2020, Icar, 348, 113777
Naidu, S. P., Margot, J.-L., Taylor, P. A., et al. 2015, AJ, 150, 54
Nakano, R., & Hirabayashi, M. 2020, ApJL, 892, L22
Nolan, M. C., Howell, E. S., Scheeres, D. J., et al. 2019, GeoRL, 46, 1956
Ostro, S. J., Margot, J.-L., Benner, L. A. M., et al. 2006, Sci, 314, 1276
Pohl, L., & Britt, D. T. 2020, M&PS, 55, 962
Pravec, P., Harris, A., & Warner, B. 2008, in IAU Symp. 236, Near Earth Objects, our Celestial Neighbors: Opportunity and Risk, ed. G. B. Valsecchi, D. Vokrouhlický, & A. Milani (Cambridge: Cambridge Univ. Pres), 167
Pravec, P., & Scheirich, P. 2018, in 42nd COSPAR Scientific Assembly (Pasadena, CA), S.3–4–18
Pravec, P., Scheirich, P., Kušniráka, P., et al. 2006, Icar, 181, 63
Raducan, S. D., Davison, T. M., & Collins, G. S. 2020, P&SS, 180, 104756
Raducan, S. D., Davison, T. M., Luther, R., & Collins, G. S. 2019, Icar, 329, 282
Raducan, S. D., Jutzi, M., Davison, T. M., et al. 2022, IJIE, 162, 104147
Rainey, E. S. G., Stickle, A. M., Cheng, A. F., et al. 2020, IJIE, 142, 103528
Richardson, D. C., Leinhardt, Z. M., Melosh, H. J., & Michel, P. 2002, in Asteroids III, ed. W. F. Bottke et al. (Tucson, AZ: Univ. Arizona Press), 501
Richardson, J. E., Melosh, H. J., Lisse, C. M., et al. 2007, Icar, 191, 176
Rivkin, A. S., Chabot, N. L., Stickle, A. M., et al. 2021, PSJ, 2, 173
Roberts, J., Barnouin, O., Daly, M., et al. 2021, P&SS, 204, 105268
Sánchez Lana, D. P., & Scheeres, D. J. 2018, AAS, DPS Meeting, 50, 312.14
Sánchez, P., & Scheeres, D. J. 2014, M&PS, 49, 788
Sánchez, P., & Scheeres, D. J. 2018, P&SS, 157, 39
Scheeres, D., Hartzell, C., Sánchez, P., et al. 2010, Icar, 210, 968
Scheeres, D. J. 2015, Icar, 247, 1
Scheeres, D. J., French, A. S., Tricarico, P., et al. 2020, SciA, 6, eabc3350
Scheeres, D. J., McMahon, J. W., French, A. S., et al. 2019, NatAs, 3, 352
Schwartz, S. R., Richardson, D. C., & Michel, P. 2012, Granular Matter, 14, 363
Soldini, S., Takanao, S., Ikeda, H., et al. 2020, P&SS, 180, 104740
Stickle, A. M., Bruck Syal, M., Cheng, A. F., et al. 2020, Icar, 338, 113446
Stickle, A. M., Rainey, E. S. G., Bruck Syal, M., et al. 2017, Procedia Engineering, 204, 116
Sugita, S., Honda, R., & Morota, T. 2019, Sci, 364, 252
Tardivel, S., Sánchez, P., & Scheeres, D. J. 2018, Icar, 304, 192
Tatsumi, E., & Sugita, S. 2018, Icar, 300, 227
Taylor, P. A., Howell, E. S., Nolan, M. C., et al. 2012, AAS Meeting, 220, 128.02
Walsh, K. J., Jawin, E. R., Ballouz, R.-L., et al. 2019, NatGe, 12, 242
Walsh, K. J., Richardson, D. C., & Michel, P. 2008, Natur, 454, 188
Walsh, W. J., & Jacobson, S. A. 2015, in Asteroids IV, ed. P. Michel et al. (Tucson, AZ: Univ. Arizona Press), 375
Watanabe, S., Hirabayashi, M., Hirata, N., et al. 2019, Sci, 364, 268
Wiggins, S. E., Johnson, B. C., Bowling, T. J., et al. 2019, JGRE, 124, 941
Wünnemann, K., Collins, G. S., & Melosh, H. J. 2006, Icar, 180, 514
Yu, Y., Cheng, B., Hayabayashi, M., Michel, P., & Baoyin, H. 2019, CeMDA, 131, 51
Yu, Y., & Michel, P. 2018, Icar, 312, 128
Yu, Y., Michel, P., Hirabayashi, M., et al. 2018, AJ, 156, 59
Yu, Y., Michel, P., Schwartz, S. R., et al. 2017, Icar, 282, 313
Zhang, Y., Michel, P., Richardson, D. C., et al. 2021, Icar, 362, 114433
Zhang, Y., Richardson, D. C., Barnouin, O. S., et al. 2017, Icar, 294, 98